Towards Autonomous Driving at the Limit of Friction

by

Sirui Song

A thesis
presented to the University of Waterloo
in fulfillment of the
thesis requirement for the degree of
Master of Applied Science
in
Mechanical Engineering

Waterloo, Ontario, Canada, 2014

I hereby declare that I am the sole author of this thesis. This is a true copy of the thesis, including any required final revisions, as accepted by my examiners.

I understand that my thesis may be made electronically available to the public.

Abstract

Autonomous vehicles have become a reality, many vehicles have implemented some features to allow partial or full autonomy; however, full autonomous driving near the limit of friction still presents many obstacles, especially near the limit of friction.

Autonomous test vehicles are expensive to build and maintain, running the vehicles usually requires highly specialized training, and testing can be dangerous. Research has shown that small sized scaled vehicles may be used as an alternative to full size vehicle testing. The first part of this thesis presents the construction of a $1/5^{th}$ scaled vehicle testbed. This testbed is inexpensive to construct, easy to maintain, and safe to test compared to full size vehicles. In the linear region, the dynamic response of the tires also closely mimics full size tires and the Dugoff tire model. The small sized testbed is therefore an ideal alternative to full size vehicles.

The interaction between the road and the tires remains a challenge to estimate, but a requirement for effective control. Tire dynamics are highly non-linear, and are dependent on many variables. Tire slip angles are difficult to estimate without expensive sensors set-up. Many linear and non-linear estimation methods have been developed to tackle this problem, but each having its limitations. The second part of the thesis presents a method for slip angle estimation, and proposes an observer design which integrates a linear component with the Dugoff tire model and a pneumatic trail estimator. This design is fast to operate, and does not require expensive sensors. With the addition of the pneumatic trail block, accurate slip angles can be obtained in the tires linear and saturation regions equally.

Controlling near the limit of friction requires consistently accurate tire states, which is difficult to achieve with slip angles. With the margin of error under a degrees, a slight error in slip angle estimates while operating at the limit of friction may result in loss of control. The final contribution of this thesis proposes a simplified feedforward lateral controller based on the concept of Centre of Percussion (COP), and a longitudinal controller that operates based on lateral acceleration. This control scheme avoids using slip angles, but still pushes the vehicle performance to the limit of friction. The architecture is validated in high fidelity simulations.

Acknowledgements

I would like to thank my supervisors, Professor Steven Waslander, and Professor Jan Huissoon, for their invaluable insights and teaching. Without them, this thesis would not have been possible. Their advise, both technical and professional, will continue to guide me in the future.

I would also like to thank all the Waterloo Autonomous Vehicle Laboratory members: Arun Das, Kevin Ling, Nima Mohajerin, Neil Mathew, James Servos, Adeel Ahktar, Michael Smart, Dr. Michael Tribou, Sid Ahuja, and Abdel El Bably. They are great minds to collaborate with, and are very supportive and helpful.

During my master's, I've had the pleasure to work with many UW co-op students, UW Robotics team members, and classmates. I appreciate all the late nights and weekends they put in making the testbed and the Robot Racer with me. I would like to especially thank Andy Wong and Michael Chi for helping me in deriving the vehicle estimation and control algorithms. It was my great pleasure to work with them.

Lastly, I would like to thank my parents and my friends for their continuous support and encouragement in the past two years. I would like to thank Vickie for bearing with me through many sleep deprived nights and encouraging me during the stressful days. I couldn't have done it without you.

Dedication

This thesis is dedicated to my family, for their love, encouragement and support.

Table of Contents

List of Tables

List of Figures

Nomenclature

α	Tire slip angle
β	Vehicle side slip angle
δ	Steering angle
$\Delta\psi$	Heading error
κ	Longitudinal slip ratio
μ	Coefficient of friction
C_α	Cornering stiffness
C_κ	Coefficient for longitudinal slip
e_{cop}	Lateral error at the centre of percussion
F_{yf}	Lateral force produced by the front tires
F_{yr}	Lateral force produced by the rear tires
I_f	Inverse peak force
I_z	Moment of inertia of the vehicle around Z axis
K	First curvature of the road
l_f	Distance from CG to the front axle
l_r	Distance from CG to the rear axle
m	Mass of the vehicle

M_z	Tire alignment moment
r	Yaw rate
s	Vehicle travelled distance
t_m	Mechanical trail
t_p	Pneumatic trail
V_x	Longitudinal velocity

Chapter 1

Introduction

Despite continuous and concerted efforts in improving passenger vehicle safety over the last century, it is expected that approximately 1.24 million deaths will occur worldwide in 2014, with another 50 million non-fatal injuries. [23] The majority of these traffic accidents are caused by human error, and can therefore potentially be avoided. The goal and promise of autonomous driving is exactly this, to save lives by removing human error from the everyday commute for millions of humans around the globe. Analysis showed that 92.3 percent of crashes in 2005-2007 were attributed to errors made by drivers [3], self driving cars have the potential to eliminate virtually all of the driver errors and most of the crashes [21].

In the recent years, many automotive manufacturers have implemented features that enable some form of autonomy on their offerings: Mercedes, BMW, Honda, Ford offer driver assisted technologies including adaptive cruise control, lane-keep assist, low-speed collision avoidance, self-park, blind-spot detection. Recently, Tesla Motors introduced the model D that can autonomously drive to the owner's location.

Recent research has shown that fully autonomous vehicles have became a reality. Audi recently demonstrated its RS7 autonomously driving around the Hockenheim track, reaching speed of 190mph [2]. The VisLab group has developed an autonomous vehicle that drove from Italy to China, journeying over 13,000km [6]. The Google car has logged over 500,000 miles of autonomous driving with no accident under computer control [22]. In fact, in as early as 2007, researchers from Carnegie Mellon University have developed BOSS, shown in Fig. 1.1; which won the DARPA Urban Challenge. It uses a trajectory rollout motion planner designed for urban driving [31].

Even with all these success stories, there are still many obstacles ahead before au-

Figure 1.1: From Left to Right: BOSS Autonomous Vehicle [31], VisLab Autonomous Vehicle [6], Google Autonomous Vehicle [30], Audi TTS "Shelley" Autonomous Vehicle [12]

tonomous vehicles are driving on the roads. Autonomous vehicles still cannot compete with human drivers in many ways, including perception of the environment and emergency evasive manoeuvres, when tires are at the limits of friction. One of the challenges in autonomous vehicle control is in professional racing, when tires are at the limit of friction. In 2012, the research vehicle, "Shelley", [12], demonstrated that by learning and adapting to the vehicle and tire dynamics, stable vehicle control near the limit of tire friction is possible.

Tire dynamics are non-linearly dependent on many varying parameters, including the slip angle, the coefficient of friction, the load distribution and tire conditions. Therefore, mathematically modelling the dynamics of a particular tire, in real time, is very difficult [25]. There exists a need to develop a practical method of vehicle state estimation & control at the limit of friction.

In addition to being difficult to model, testing any new control method that pushes the vehicle to its limits presents many practical challenges. Firstly, autonomous driving test vehicles are expensive to build, sometimes on the order of millions of dollars. Secondly,

these vehicles may require specialized team for maintenance and repair. Lastly, testing in these vehicles can be dangerous.

There exists a need to develop a suitable small scale autonomous driving platform that can model full scale vehicle dynamics, while minimizing costs, requirement for specialized staff, and reduces the possibilities for injuries.

1.1 Related Work

From the descriptions in the previous section, the problems can be categorized into three research areas: designing a small scale autonomous driving platform, vehicle state estimation, and vehicle control near the limit of friction.

1.1.1 Small Scale Vehicle Platform

The main benefits of using a small scale vehicle testbed, compared to a full scale vehicle are that the vehicle is easy to design, build, test, and repair. It allows also for multiple vehicles to be tested autonomously together with ease. Many research facilities have already implemented similar set-up to do their research.

Some of the most influential work published on scale vehicle dynamics was conducted at Urbana-Champaign on the Illinois Roadway Simulator (IRS) [8]. One of the key conclusions from the testbed was that the model dynamics were similar to those of full scale vehicles in the linear range.

More recently in 2009, Lapapong et al. developed and experimented with similar scaled testbed, Pennsylvania State University Rolling Roadway Simulator (PURRS), [19]; see Fig 1.2. Similar to the study done at IRS, a scale vehicle was built and tested on a treadmill, and data was gathered from a sensing arm. This research determined there is a good correlation on vehicle dynamics between full scale vehicles and with scaled vehicles for low to medium frequency input. At higher frequencies, poor correlations between the small scale platform and the full size vehicle were observed. This is attributed to the tires used on the scaled platform. Since the wheels chosen were made of solid rubber, they are too stiff to simulate the tire lag dynamics that exist in full scale pneumatic tires.

In 2011, Jakobsen presented a project that uses a $1/5^{th}$ scale model car to test autonomous drifting controllers [16]. It identified various methods to characterize the vehicle dynamics and tire dynamics. In simulation, Jakobsen also demonstrated promising results

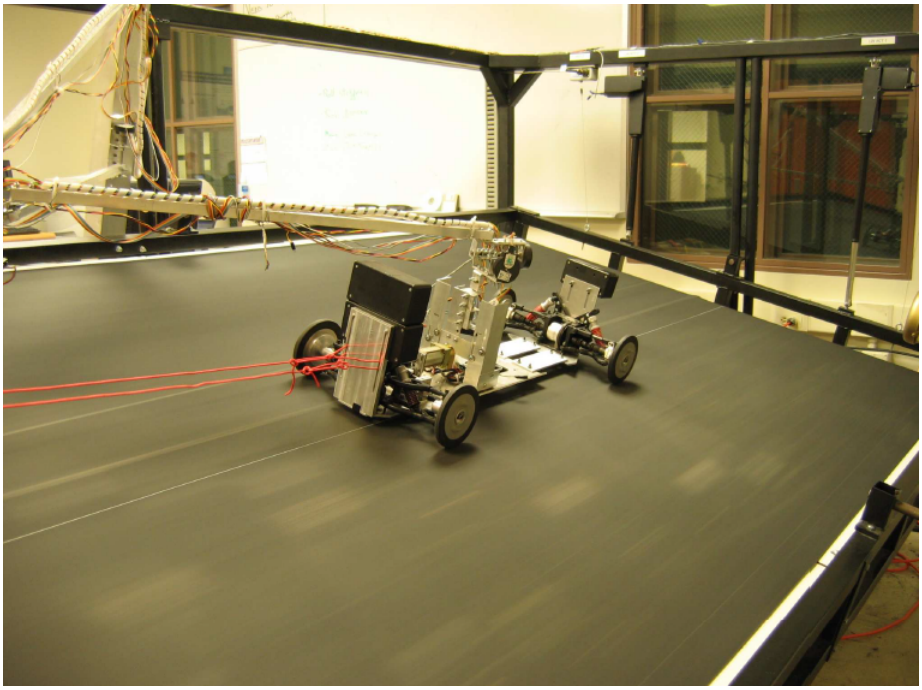

Figure 1.2: Pennsylvania State University Rolling Roadway Simulator [19]

in using the small scale platform as a testbed for drift control [16]. The platform, however, relies on the ground station to record and process vehicle state data, this latency in communication may not be suitable for controlling a vehicle near the limit of friction, where timing is critical.

Andrew Liburdi built a 1/10th scale vehicle [20], and parametrized the tire dynamics to simulate real vehicles. The platform is shown in Fig. 1.3. This study compared the dynamic performance of scaled vehicle to the full size vehicle using dimensional analysis(Buckingham Pi Theorem), it was found that the distribution of the Pi group and the actual tire dynamics are very similar, indicating a quantitative matching between scale and full size tire response. The key difference of this research is that all control and acquisition systems are now built into the vehicle itself, thus minimizing the requirement of additional equipment (treadmill etc.) and lab space. With a self-contained platform, there are no restrictions on the type of manoeuvres performed.

As the vehicle size increases, the discrepancies in dynamic response relative to large vehicles diminishes. In this work, we develop a $1/5^{th}$ scale autonomous vehicle testbed which combines the benefits of smaller test platforms such as safety and ease of use with

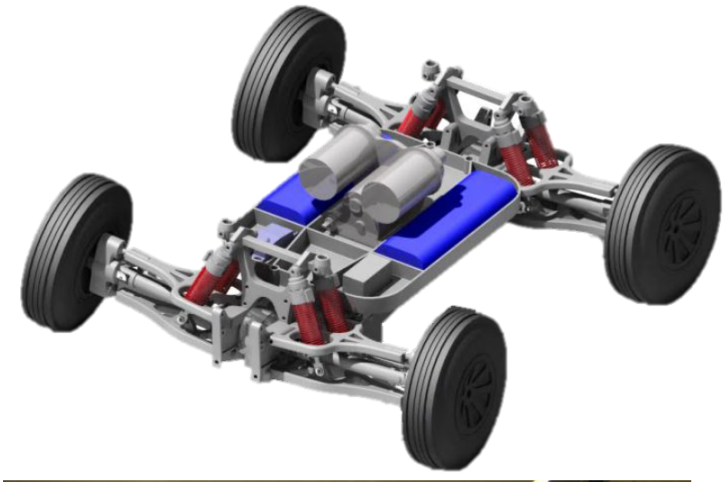

Figure 1.3: $1/10^{th}$ Scaled test platform from University of Windsor [20]

dynamic response that should prove to be quite similar to full-scale vehicles.

1.1.2 Vehicle State Estimation

Given the importance of slip angle and longitudinal slip in predicting vehicle dynamics, researchers have attempted to estimate these parameters. Slip angle can be calculated using accurate Global Positioning System (GPS) and Inertial Measurement Unit (IMU) measurements.

In 2006, J. C. Gerdes proposed a method to measure slip angles using two RTK (real time kinematic) GPS mounted on the vehicle [7]. With sub-centimeter accuracy on each GPS sensor, position, heading and ground speed of the vehicle can be determined accurately. This method allows accurate slip angle measurement with only simple filtering techniques. However, this method uses specialized sensors. Due to its high sensitivity to noise, this method cannot be used with low-cost sensors available on most commercial vehicles. Motivated by this need, other estimation/observer algorithms have been proposed.

A common type of estimation method proposed for autonomous driving applications is an Extended Kalman Filter (EKF). In [10] and [33], an EKF is designed to estimate the slip angles and longitudinal slips of the tires. The work presented in [10] demonstrates that the EKF performs well in the linear tire region, but is fails to track accurately in the

non-linear region. Furthermore, fast convergence of the EKF is highly dependent on the accurate selection of tire parameters and vehicle models.

Linear observers have also been proposed for vehicle state estimation. This structure is used in many papers to capture the linear tire dynamics well, and in some cases is even able to quickly converge to an accurate estimate in the non-linear tire region [14, 10, 4].

In order to increase accuracy of tracking in the non-linear tire region, other estimation techniques have been explored. For example, a Particle Filter (PF) is able to provide more accurate estimates of slip angles, but is computationally intensive, and thus difficult to implement in real-time [33]. Another approach, using the Unscented Kalman filter (UKF), is described in [11]. While the results are promising, this estimator design is dependent on several unconventional sensors that are not commonly found on commercial vehicles.

Recent efforts have demonstrated the benefit of using pneumatic trail to estimate tire-road behaviours, such as estimating the friction coefficient and lateral tire forces [34, 15]. The pneumatic trail is a tire property encoded in the alignment moment measurements. In [15], it was found that a linear observer coupled with a pneumatic trail estimator, can accurately track the sideslip angles in both the linear and non-linear regions. Furthermore, this method is less reliant on the accuracy of model and tire parameters, uses simple calculations, and only requires sensors that are available on most commercial vehicles. However, the method presented in [15] assumes a rear wheel drive vehicle, and negligible longitudinal dynamics on the wheels. Neglecting longitudinal tire dynamics limits the accurate tracking of slip angles to areas near the horizontal axis of the slip circle. In additions, for most vehicles, especially front wheel drive vehicles, tire saturation occurs much earlier with longitudinal tire dynamics present. For example, in an emergency braking situation, the vehicle may steer and rapidly decelerate at the same time. Inaccurate slip angle estimates in this situation may lead to loss of control.

This thesis describes an estimation method which allows accurate slip angle tracking, even under heavy longitudinal acceleration.

1.1.3 Vehicle Control near the Limit of Friction

In most cases, vehicle speed (longitudinal) and vehicle heading (lateral) are controlled separately. For example, in [9, 29], a proportional controller is used to control steering angle, while a separate controller is used to maintain desired speed. One example of this was the Pure Pursuit controller. The steering wheel is generated based on some the lateral error a certain distance ahead on the track. This method works very well for control at low speed, where the vehicle behaves linearly for the most part. However, this method

fails when track or vehicle dynamics are involved. As shown in [28], depending on the gain setting, the Pure Pursuit method tracks a "Figure-eight" with large oscillations, or with large lateral errors.

In 2005, the Stanley lateral controller was introduced [29]. It uses the front axle as a reference point, and uses both lateral error, and heading error to regulate the steering angle. This model significantly reduces the oscillatory motion. However, since the underlying vehicle model is kinematic, it fails to track closely when the vehicle is accelerating.

Using a dynamic vehicle model, vehicle behaviours can be more closely modelled. In most cases, vehicle dynamics can be modelled as a single track bicycle model while still capturing the major dynamic effects. However, due to its non-linearity, tire dynamics cannot be easily modelled.

Many linear controllers use a simplified linear tire model to avoid this problem. While this is a valid technique for low speed modelling, it often fails when tire forces are saturated, and tire forces become significantly non-linear. Other researchers [32] have used non-linear techniques to capture the non-linear tire dynamics. However, non-linear techniques improves the performance of the controller only when all measurements are estimated accurately. As described in the previous section, in practice, measurements, such as slip angles, are difficult to obtain. Furthermore, non-linear controllers are generally much more computation intensive.

Drawing a compromise between the accuracy of the tire model and computation time, J. Gerdes and K. Kritayakirana has developed the controller implemented on the Shelley autonomous vehicle [17]. This controller pushes the vehicle performance near the tire friction limit, by using a Dugoff tire model. It is divided into a lateral controller and a longitudinal controller. The Lateral controller is assumed to always take priority in allocating the tire available forces.

The lateral controller consists of a feedback and a feedforward term. The feedback is implemented in a full state feedback structure with four states: lateral error, heading errors and their derivatives. The feedforward term employs a concept called Centre of Percussion (COP). When turning, the tires on a vehicle generate both a lateral force, and a yaw moment about the centre of mass. the centre of percussion with respect to the rear tires, refer to a point where the effects produced by the lateral forces and the yaw moment cancel each other out, resulting with zero lateral acceleration. This is illustrated in Fig. 5.2. Using the centre of percussion with respect to the rear tires, as a reference point, [17] simplifies the calculation for lateral error.

The longitudinal controller monitors lateral slip angle and longitudinal vehicle slip. Using a Dugoff tire model, the controller computes how much tire forces are available, and

translate that into a desired speed. The longitudinal controller also monitors a referenced desired speed. Lastly, the controller tracks a desired acceleration profile. These three outputs are weighted and a desired output is calculated. The controller proposed in [17] has been tested on the Shelley autonomous car, and has performed well. However, this controller requires accurate slip angle feedback in order to perform well. When slip angle data is not accurate, the stability of the controller is compromised.

This thesis describes a controller that will push the vehicle to its limit without using slip angle measurements.

1.2 Contributions and Approach

The thesis presents a low cost, low maintenance test platform for vehicle dynamics testing; this is especially suitable for higher risk tests. The thesis presents the hardware and software architecture for the small scaled test platform. It also presents experimental results on the tire and vehicle models. It is determined that the dynamics of the small platform exhibit similar response as compared to full scale vehicles. With the vehicle parameters determined, both estimation and control tests can be performed using this platform.

In order to obtain accurate slip angle estimates, a pneumatic trail based observer design with longitudinal tire dynamics is presented. By accounting for the longitudinal dynamics, this method extends accurate slip angle estimates to the full domain of the slip circle. This observer design improves on the previous methods in two distinct areas: first, it can accurately estimate slip angle in both linear and non-linear regions, even with high longitudinal dynamics present; second, it can be implemented for both front wheel drive and rear wheel drive vehicles. In addition to the benefits, this observer design still uses a simple model that is not computationally intensive, and only requires input from commonly available sensors to operate.

For vehicle control near the limit of friction, an alternative way to control the vehicle, while maximizing its performance and maintaining stability is presented. Unlike previously proposed control methods, this controller does not require lateral slip angle, α, to operate. This reduces the complexity of the controller design, and no longer requires a sophisticated slip angle estimation algorithm, or an expensive sensor to be present. Furthermore, the controller can be used in front, rear or four wheel drive vehicles, as long as longitudinal slip ratio is provided.

1.3 Thesis Outline

In Chapter 2 of this thesis, vehicle and tire dynamics models are outlined, and the concept of pneumatic trail is introduced. The $1/5^{th}$ scale autonomous testbed architecture and test results are presented in Chapter 3. The pneumatic trail estimator and simulation and experimental results are discussed in Chapter 4. In Chapter 5, the architecture and test results of the controller are described in detail. Conclusions and recommendations are listed in Chapter 6.

Chapter 2

System Modelling

2.1 Single Track Bicycle Model

One of the simplest vehicle models is the single track bicycle model, as shown in Fig. 2.1. This model combines the left and right wheels on each axle into two wheels along the vehicle centre axis. This simplification limits the model's ability to account for any longitudinal weight transfer, lateral weight transfer, or vertical dynamics due to suspensions; furthermore, any torque steering effect, lateral torque vectoring cannot be accounted for with this model. In order to account for these dynamics, a double track vehicle model can be used [32].

The benefits of the single track vehicle model is that it can easily calculate the longitudinal and yaw motion of a vehicle. Due to its simplicity, this model is extensively used in controller and estimator designs, where computation power is usually limited, but fast calculations are required.

The major assumptions used in the kinematic bicycle model is that the rear tire is aligned with the body motion, and front tire is aligned with the steering angle. This is equivalent to assuming that slip angles at both wheels are zero. This assumption is reasonable at low speeds, when lateral forces generated are small, (less than 5 m/s) [25].

The overall equation of motion is shown in Eq. (2.1):

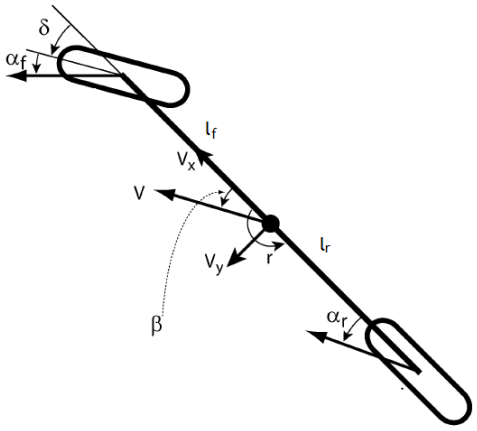

Figure 2.1: Single track bicycle model [15]

$$\begin{aligned} \dot{X} &= V_x \cos(\psi + \beta) \\ \dot{Y} &= V_x \sin(\psi + \beta) \\ r &= \frac{V_x \cos(\beta)}{L} \tan(\delta) \end{aligned} \tag{2.1}$$

where X and Y are the global positions respectively. V_x is the longitudinal velocity of the vehicle, ψ is the global heading of the vehicle, β is the vehicle side slip angle, explained in 2.2, L is the wheelbase, r is the yaw rate measured from the vehicle body coordinate, and δ is the steering angle.

The dynamic bicycle model uses tire forces to calculate the lateral accelerations and yaw dynamics of the vehicle. The equations are shown in Eq. (2.2) and Eq. (2.3).

For lateral motion only:

$$\begin{aligned} m(\ddot{y} + V_x r) &= F_{yf} + F_{yr} \\ I_z \dot{r} &= l_f F_{xf} - l_r F_{yf} \end{aligned} \tag{2.2}$$

where F_{yf} and F_{yr} are the front and rear lateral force exerted by the tires. l_f is the distance from the front axle to the centre of mass, and l_r is the distance from the rear axle to the centre of mass.

For longitudinal motion only:

$$m\ddot{x} = F_{xf} + F_{xr} \tag{2.3}$$

where F_{xf} and F_{xr} are the front and rear longitudinal force exerted by the tires.

2.2 Slip Angle and Slip Ratios

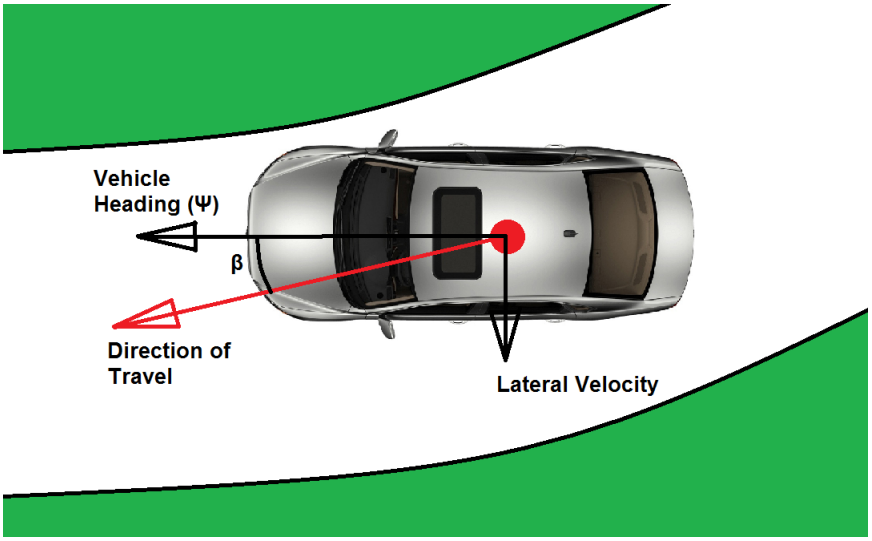

Figure 2.2: Illustration of vehicle side slip

Vehicle side slip angle, shown in Fig. 2.2, is defined as the angle difference between the direction of travel, and the vehicle heading. The slip angle calculated from a kinematic bicycle model is shown in Eq. (2.4).

$$\beta = tan^{-1}(\frac{l_f \tan\delta}{L}) \tag{2.4}$$

where l_f is the distance between centre of mass and the front axle.

For the dynamics model of the vehicle slip angle, the vehicle side slip angle β, Eq. (2.5), which uses the small angle assumption.

$$\beta = \frac{\dot{y}}{V_x} \tag{2.5}$$

Front and rear tire slip angles, α_f and α_r, can be related to the body side slip angle β by the following equations:

$$\alpha_f = \delta - \beta - \frac{l_f r}{V_x} \tag{2.6}$$

where δ is the steering angle, and r is the yaw rate of the vehicle.

$$\alpha_r = -\beta + \frac{l_r r}{V_x} \tag{2.7}$$

The longitudinal slip ratio is given by Eq. (2.8) and is the difference between the velocity of the wheel and the velocity of the vehicle.

$$\kappa = \frac{V_{xt} - V_x}{|\max(V_{xt}, V_x, \epsilon)|} \tag{2.8}$$

where V_{xt} is the velocity of the wheel, calculated as the product of the effective tire radius and the wheel rotational speed; V_x is the longitudinal velocity of the vehicle; and ϵ is a constant parameter with a small value so the denominator is not zero.

For a front wheel drive vehicle, the rear wheel does not apply driving force, longitudinal effects for the rear tires are generated by friction. For most cases, this is negligible compared to the front driving tires. We make the assumption that the longitudinal slip ratio on the rear tire is zero, or the rear tires do not slip. Therefore, the front tires slip ratio becomes Eq. (2.9). This calculation assumes accurate knowledge of velocity, and is only valid when the rear wheels experience negligible longitudinal slip. In cases where this does not hold true, alternative methods to estimate the slip ratio, κ, such as an EKF [10], can be used.

$$\kappa_f = \frac{V_{xf} - V_{xr}}{\max(V_{xr}, V_{xf}, \epsilon)} \tag{2.9}$$

2.3 Tire Models

For a pneumatic tire, the lateral force exerted is a function of slip angle, load, coefficient of friction and cornering stiffness. The relationship is usually non-linear, making it difficult to model. This relationship is illustrated in Fig. 2.3. At small slip angles, typically under 7 degrees, the amount of force exerted appears almost linear; while at larger slip angles, typically 8 to 10 degrees, tire force reaches its peak, and plateaus; any further increase in slip angle decreases the amount of force exerted. Furthermore, the different cures indicate

vertical loading. As axial loading on the tire increases, the peak force produced increases as well.

In professional racing, drivers try to keep the tires at its peak to maximize cornering speed. If this peak is exceeded, the tires are considered fully saturated, and cornering performances decreases.

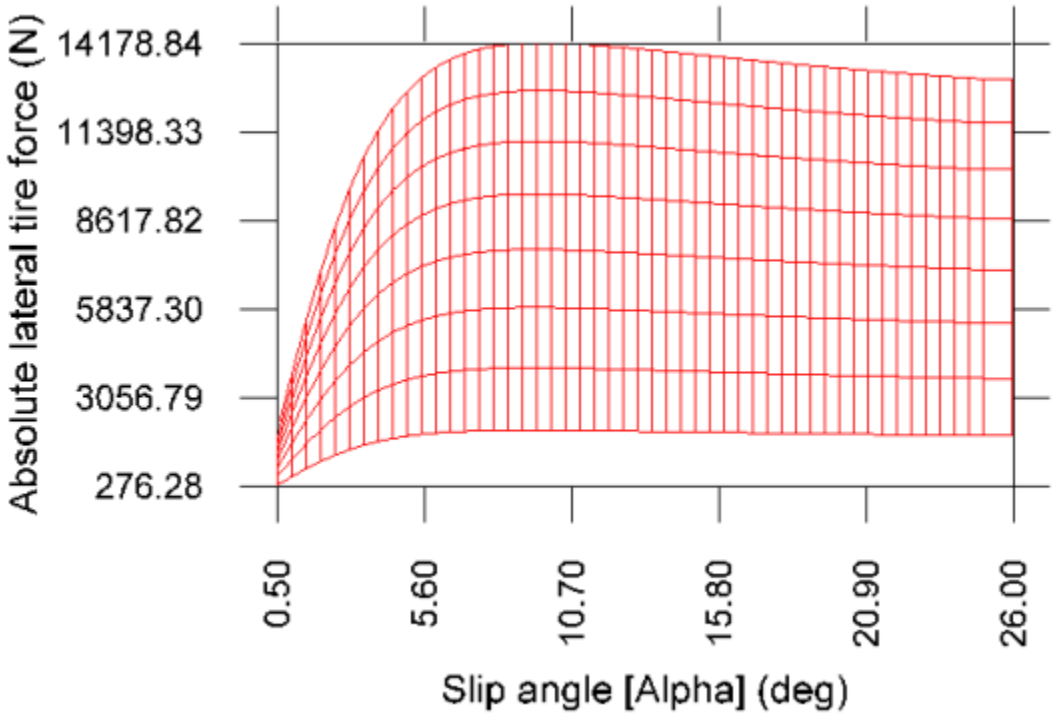

Figure 2.3: Lateral force vs. slip angle illustration for a typical tire [13]

The longitudinal tire dynamics are similar to that of the lateral dynamics. The longitudinal force exhibit the similar non-linear response with respect to slip ratio, κ.

2.3.1 Linear Tire Model

Linear tire models assume that the relationship between slip angles and forces is linear. For the lateral dynamics, this is modelled by a constant cornering stiffness coefficient, C_α. For longitudinal dynamics, this relationship is represented by C_κ. As observed in Fig. 2.3,

at low slip angles or slip ratios, this assumption is valid; thus, this model can be used for controller or estimation purposes at low speed. However, when tires are more saturated, this assumption would no longer hold true.

$$\begin{aligned} F_x &= -C_\kappa \kappa \\ F_y &= -C_\alpha \alpha \end{aligned} \tag{2.10}$$

2.3.2 Dugoff Tire Model

The Dugoff tire model [25] is a simple analytical model that incorporates both longitudinal and lateral dynamics to calculate the tire-road force characteristics. It assumes a steady state tire behaviour. Compared to other well known models, such as the Fiala tire model or the linear tire model [24], the Dugoff tire model is more accurate over a larger range of operating conditions by accounting for the longitudinal tire dynamics as well as the lateral dynamics. In comparison to the more sophisticated models, such as the Pacejeka Magic Formula[24], the Dugoff tire model uses fewer parameters, and is less reliant on accurate tire parametrization. The Dugoff tire model is summarized for the front tires in Eq. (2.11)-(2.13),

$$\begin{aligned} F_{xf} &= \begin{cases} -C_\kappa \dfrac{K_D \kappa}{1+\kappa}, & a_x > 0 \\ -C_\kappa K_D \kappa, & a_x \leq 0 \end{cases} \\ F_y &= \begin{cases} -C_\alpha \dfrac{K_D \tan(\alpha)}{1+\kappa}, & a_x > 0 \\ -C_\alpha K_D \tan(\alpha), & a_x \leq 0 \end{cases} \end{aligned} \tag{2.11}$$

with

$$K_D = \begin{cases} (2-\sigma)\sigma & \sigma < 1. \\ 1, & \sigma \geq 1. \end{cases} \tag{2.12}$$

$$\sigma = \frac{(1+\kappa)\mu F_z}{2 I_f \sqrt{C_\kappa^2 \kappa^2 + C_\alpha^2 \tan^2(\alpha)}} \tag{2.13}$$

As described in[15], an observation can be made that the μ term and F_z term always appear together, in both the Dugoff tire model and the pneumatic trail calculations. The two terms can be combined together into an inverse peak force coefficients for the front and rear tires, I_f and I_r.

$$
\begin{aligned}
I_f &= \frac{1}{\mu F_{zf}} \\
I_r &= \frac{1}{\mu F_{zr}}
\end{aligned}
\tag{2.14}
$$

2.3.3 Slip Circle

Vehicle dynamics are governed by the tire-road force interaction. The maximum force generated by the tire can be illustrated through the slip circle, shown in Fig. 2.4. The horizontal axis is the normalized sideslip angle, and the vertical axis is the normalized longitudinal slip ratio. Point A, high slip ratio and low slip angle, corresponds to the case when the vehicle is accelerating. Point B, low slip ratio and high slip angle, corresponds to the case when the vehicle steers aggressively. Dotted line: vehicle driving at the limits of friction.

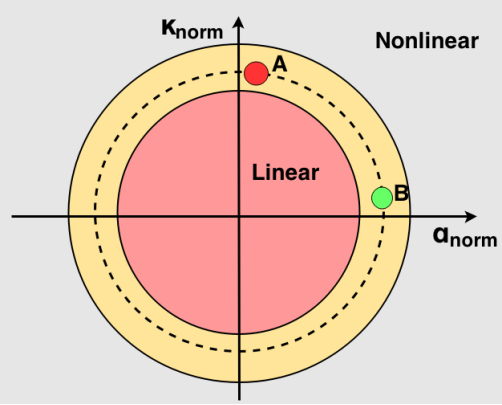

Figure 2.4: Illustration of a tire slip circle

Near the centre of the slip circle, indicated by the red region, the longitudinal slip ratio and lateral slip angle are independent of each other. Near the edge of the slip circle, in the yellow region, the longitudinal and lateral slips are no longer independent, and the produced tire force is limited by maximum friction force. Outside of the slip circle, the vehicle experiences full tire saturation, and tire performances are no longer maximized.

2.4 Aligning Moment and Pneumatic Trail

Finally, the aligning moment, or self-aligning moment, is the moment that steers the tire in the direction of vehicle travel as the tire rolls [27]; it is defined by Eq. (2.15). The aligning moment is produced, because lateral force applies at an offset from the wheel centre, due to the elastic nature of pneumatic tires. This offset is known as pneumatic trail, t_p. For vehicles with a non-vertical steering axis due to camber angle, the aligning moment applies at an additional offset, known as the mechanical trail, t_m. Fig. 2.5 and Fig. 2.6 illustrate the relationship between lateral force, F_y, pneumatic trail, t_p, and mechanical trail, t_m for a typical pneumatic tire. In this study, the focus is on pneumatic trail, and mechanical trail is assumed constant.

$$M_z = -(t_p + t_m)F_y \tag{2.15}$$

where M_z is the aligning moment. Alignment moment can be measured by monitoring the torque produced by the steering assist motor, or by torque sensors mounted on the kingpins.

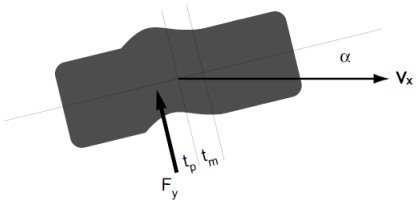

Figure 2.5: In this image, V_x is the vehicle velocity, and α is the tire slip angle. Aligning moment is produced because F_y does not apply directly at the tire's center. As the tire saturates, t_p approaches the center, and the aligning moment approaches zero. t_m is measured from the centre of the tire [15].

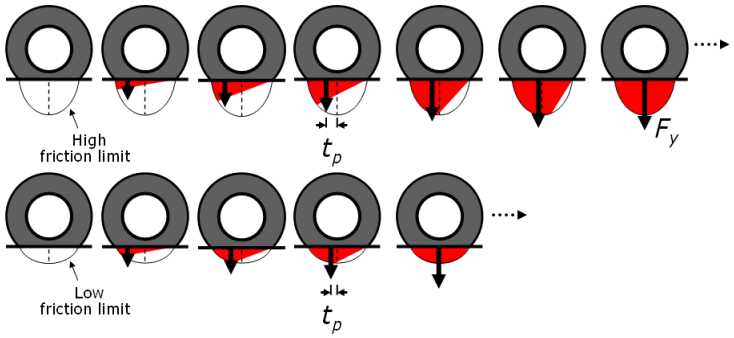

Figure 2.6: As the tire forces are saturate, pneumatic trail approaches centre of the tire [15].

In this section, the simplified single track dynamic vehicle model and the Dugoff tire model are described in details. They are simple to use, yet are able to capture most of the dynamics. The properties of alignment moment and pneumatic trail are also described; as the tires force saturates, the alignment moment approaches zero, and the pneumatic trail decreases.

Chapter 3

Testbed Characterization

3.1 Hardware Description

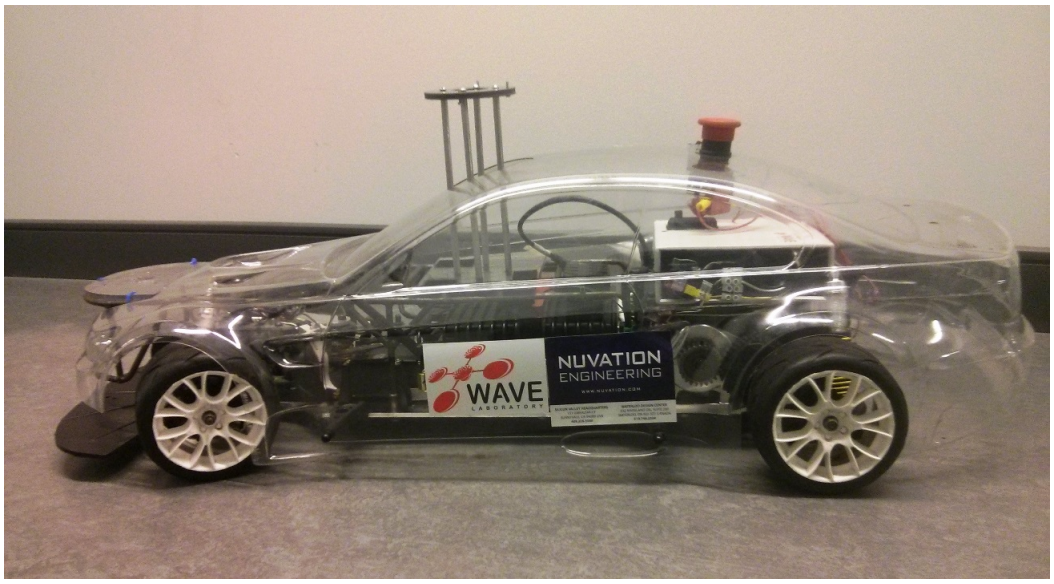

Figure 3.1: The $1/5^{th}$ scale autonomous vehicle testbed

The base platform for this autonomous vehicle testbed is a $1/5^{th}$ scale RC car, designed and built by FG Modellsport. The gas engine and the transmission have been replaced with a Mamba Monster XL ESC and Castle Creation brushless motor for improved control.

The testbed's powertrain distributes power to the wheels through the front and rear open differentials; this minimizes tire slip. The testbed is also equipped with independent double wishbone suspension to minimize vibration and improve tire grip. The testbed is four wheel drive, the motor powers the front wheels through a drive belt, and the rear through a gear train.

As described in [19], the steering response for small scale vehicles does not scale up to full size vehicles for high frequency inputs. This is due to the slow actuation from the steering servo. To improve the steering response time, the vehicle is equipped with a HiTec HS-5805MG digital servo. This servo can provide up to 24.7 kgcm of torque, and achieve a speed of 0.14s/60 degrees. With this set-up, the response time for the tires to steer from -30 degrees to 30 degrees (full left to full right) is 0.5 seconds.

The autonomous vehicle testbed is equipped with two cable-actuated disk brakes in the front, with options to install two more in the rear. The front disk brake set-up is shown in Fig. 3.2. The brakes can be retro-fitted to be controlled independently, thus providing the flexibility to implement control techniques such as torque vectoring. Currently, the brakes are used as a hard emergency stopping method: in case of a catastrophic system-wide failure, the brakes can be actuated remotely or via the on-board E-stop, independently of the on-board controllers. This added layer of security is essential for a testbed that will be used in a variety of experiments.

Figure 3.2: Disk brakes on the FG Sportline

The tires are standard rubber road tires from the FG Sportline. Compared to full size pneumatic tires, these tires are wider when scaled up. The extra surface area provides more friction force and more cornering force. The tires are non-pressurized, and the side walls

are thicker and shorter. Thus, it is expected that the tire side walls on the small scaled vehicle would be stiffer than a full size pneumatic tire, and the tire lag is less noticeable [19]. The scaled tires would be able to generate more force during very dynamic manoeuvres. However, as an autonomous vehicle testing platform, the scaled vehicle still has merits. It will be shown in Section 3.4 that the scaled and the full scale tires demonstrate similar trends in force generation. Tire dynamics can be captured by the Dugoff tire model, described in Chapter 2. As such, for controllers that operate in or near the tire's linear regions, the testbed would generate useful results. Lastly, since the small scale tires can provide more force and have simpler dynamics, it is a good validation tool for controller testing, before it is implemented on the full size vehicle, where tire lag and other higher order dynamics are more prominent.

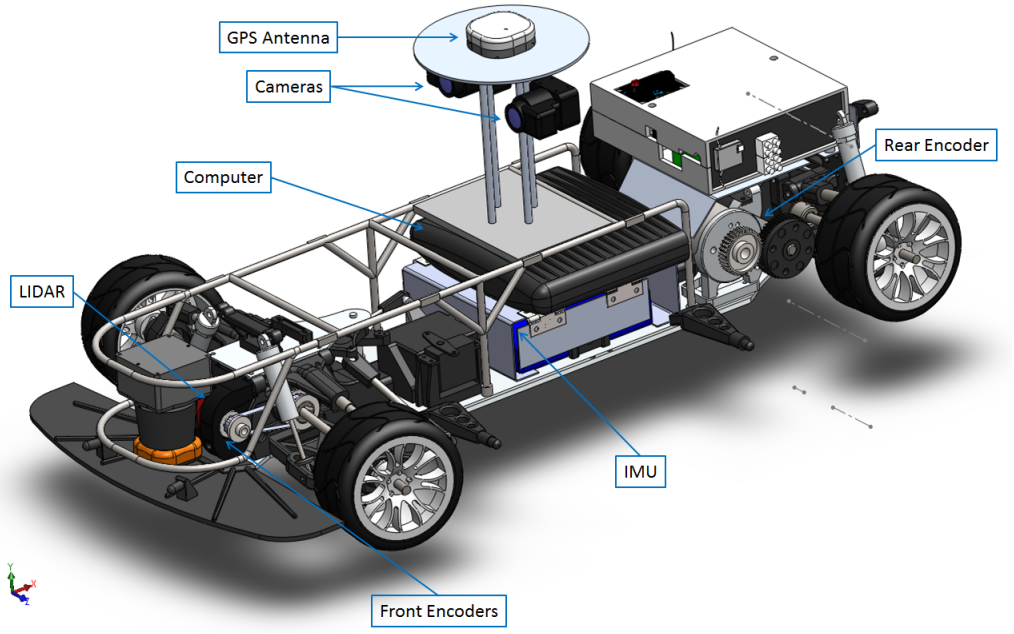

Figure 3.3: CAD drawing of the vehicle testbed

As shown in Fig. 3.3, several sensors are used on the testbed to enable autonomy. Two high resolution quadrature encoders are attached to the front wheels through a belt and pulley system. A rear motor mount encoder is used to measure the motor r.p.m. (and thus the rear wheel speed). This setup may be used to monitor wheel slip and wheel steer of the vehicle. It is also useful for torque vectoring. An absolute encoder is mounted on the steering shaft to determine the steering angle with an accuracy of 0.05 degree. A current sensor is also mounted with the steering servo in order to estimate the steering torque.

Two 2D planar LiDARs can be mounted on the testbed. They are used to map out the environment at the front and the rear. This information can be used to simulate radar inputs or to obtain ground truth. A stereo-vision camera can be added at the top of the vehicle along with a centi-metre level Real Time Kinematic GPS. This combination enables vision based research, while providing accurate position level ground truth. The heading of the vehicle is determined through a MicroStrain Inertia Measurement Unit, which can provide heading data at 200Hz with 2 degrees accuracy.

The autonomous vehicle testbed is equipped with two levels of computation. A mini-ITX sized computer with a 4th generation Core i5 CPU is mounted at the centre of the vehicle as the high level processor. This computer is useful for running sophisticated algorithms such as vision data processing, localization and mapping, non-linear estimation and control methods. The lower level processor is an Arduino Mega. It interfaces with the motor electronic speed controller, encoders, batteries, and the RC controller, and is used to handle time-critical, but simple processes such as traction control, translating signals, calculating encoder speed. The Arduino Mega is selected as the low level micro-controller for three reasons: first, it has the most open source software community support. The test platform is meant to be used on various projects, so a well documented and supported piece of hardware allows everyone on the team to easily troubleshoot problems. Second, it easily integrates with many sensors. The Arduino Mega provides four separate hardware serial communication pins, is able to accommodate both SPI and I^2C protocols, and has 15 PWM output pins; this ensures any additional sensors can be integrated easily in the future. Three, there are many shields available that easily integrate with the board. Using shields reduces development time, simplifies repair and maintenance. The communication link between the high level control and low level control is native serial communication. This communication is chosen for its ease of integration and near real-time data transfer rates. As an alternative, a real time Ethernet protocol can be used to replace the serial line. Ethernet allows much higher data throughput, but is more difficult to implement. This hardware architecture is shown in Fig. 3.4.

3.2 Robot Operating System

The overall software architecture is built on the Robot Operating System (ROS). ROS is a flexible software framework constructed in C and Python. It contains a collection of tools, libraries, and conventions that simplify the task of creating a complex robotic system [1]. First developed in 2007 at Stanford University, ROS has since become one of the most popular robotics frameworks in the world. Due to its extensive community support, ROS

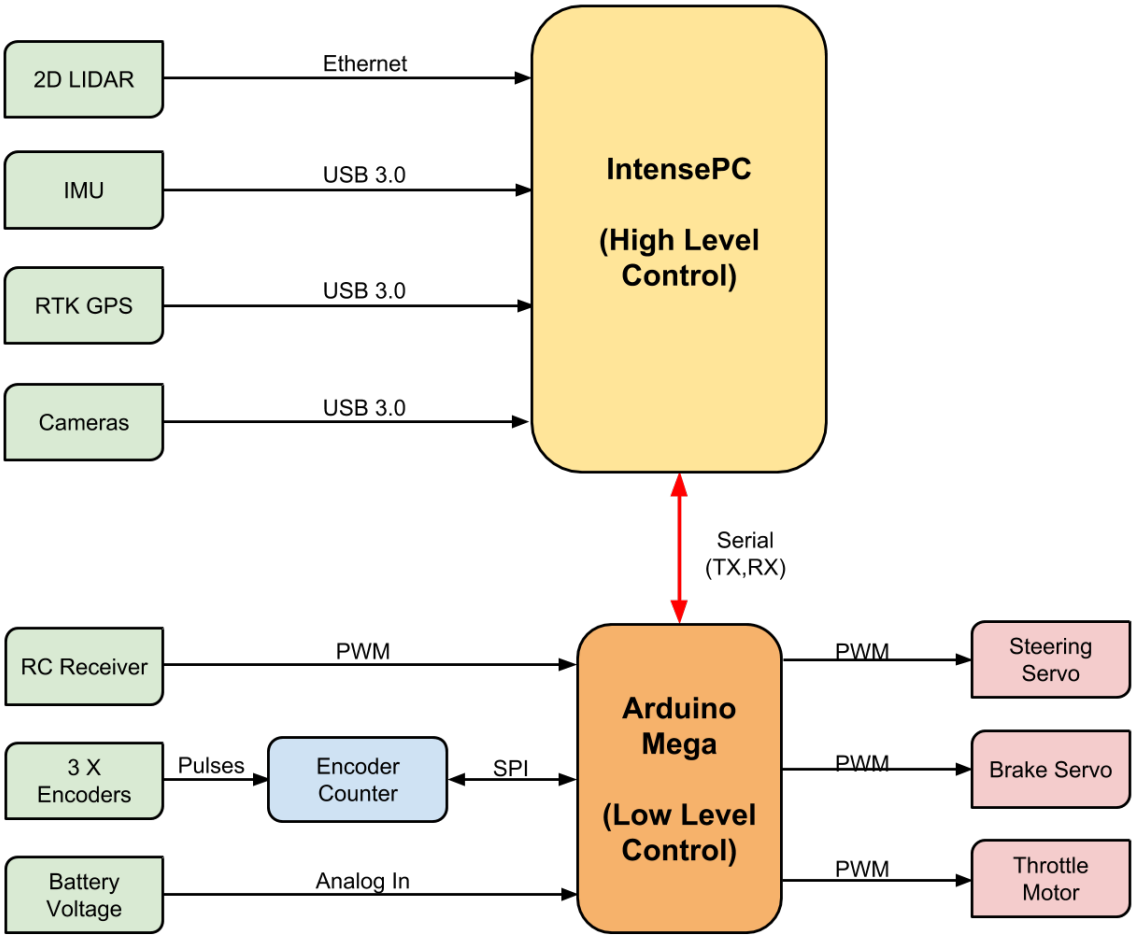

Figure 3.4: Autonomous vehicle testbed hardware architecture

has been used in various robots, such as the Clearpath Husky and the WillowGarage PR2.

Acting like an operating system, ROS enables easy and flexible interfacing with various sensors. The central piece that regulates all communications is ROSCore. In this system, each sensor has its own ROS device driver, appearing as a ROSNode. These ROSNodes communicate with the ROSCore through standard ROS Messages. Communication between nodes are established through "publishing" and "subscribing". Any node can specify that type and name of the messages it wants to receive, by subscribing the request to ROSCore. When a node publishes the exact message requested, ROSCore relays the message to the requested ROSNode. Since the message types are standardized, switching and replacing any sensor on the system is as easy as changing the requested ROS

message name.

In order to accommodate the various sensors and systems used in the field of robotics, ROS comes with many standardized message types; some of the ones used in the current system set-up are listed below in Table 3.1

Table 3.1: ROS Messages used in the vehicle testbed

Sensor	**ROS Message Type**
GPS	Geometry_Msgs/Pose
IMU	Sensor_Msgs/IMU
LiDAR	Sensor_Msgs/LaserScan
Encoders	Std_Msgs/Float32

Many fundamental algorithms, such as path planner, linear controllers, laser mapping have already been integrated into the ROS framework. Similar to the sensor ROSNodes, each algorithm can be acting in its own ROSNodes. For example, one can easily switch a PID linear controller to a more sophisticated non-linear controller for velocity control, simply by subscribing to a different set of messages. This process is illustrated in Fig. 3.5.

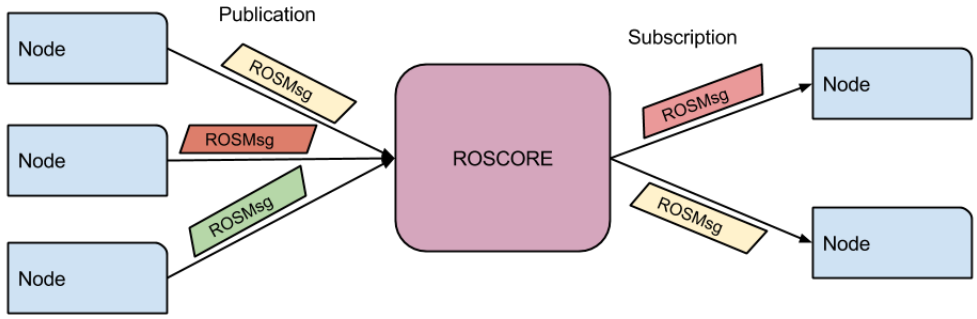

Figure 3.5: ROS Core and ROS Nodes

As a testing platform, ROS enables quick and easy integration of various sensors and algorithms. The result is a very scalable, modular, and flexible platform that can test most common sensors and algorithms.

3.3 Vehicle Characterization

The centre of gravity is determined in high fidelity CAD models, shown in Fig. 3.3. It is then verified by balancing the vehicle on a small cylindrical 5mm diameter rod. It is determined that the weight and centre of gravity measured is within 1cm to the high fidelity CAD model. It is assumed that the mass moment of inertia around the z axis, $I_z z$ determined by the CAD model would be accurate. Table 3.2 shows the static parameters determined for the $1/5^{th}$ scaled test platform.

Table 3.2: Static parameters for the $1/5^{th}$ scaled test platform

Parameters	$1/5^{th}$ **Scale**	**Full Scale**
mass $[kg]$	12	2300
CG to front axle $[m]$	0.23	1.5
CG to rear axle $[m]$	0.27	1.5
Moment of Inertia $[kgm^2]$	0.27	1.5

3.4 Tire Characterization

One of the most important aspect in system identification is estimating how much lateral force the tires are able to generate. As mentioned in section 2.3, tires generate lateral forces as a non-linear function of slip angles. By estimating tire slip angles accurately, tire forces and thus vehicle dynamics can be estimated more accurately.

In order to determine the non-linear tire curve, slip angles and lateral forces need to be measured accurately.

From equations (2.6) and (2.7), calculating the tire slip angles requires longitudinal speed measurement V_x, yaw rate, r, and vehicle side slip angle, β.

V_x is determined through the encoder reading, r is measured from the on board IMU. A definition of the vehicle side slip angle is the angle difference between the vehicle heading and the direction in which the vehicle is travelling.

In order to obtain accurate vehicle heading and position information, the vehicle was placed under an Optitrack indoor positioning systems (IPS). The IPS is able to track

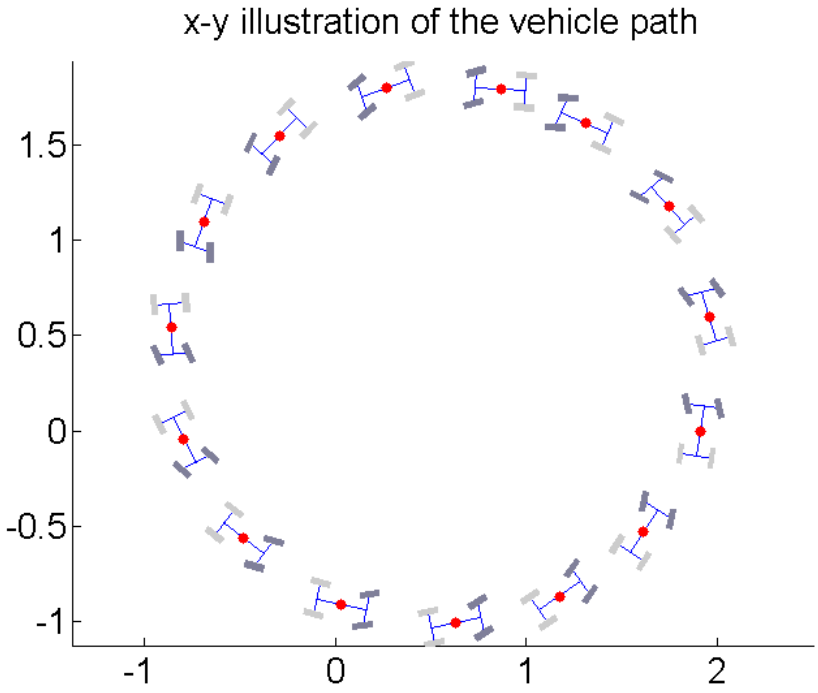

Figure 3.6: X-Y Position plot of the test vehicle for tire characterization

vehicle position to within a millimetre and vehicle heading to within 0.1 degree. Vehicle travelled direction for each time step can be calculated accurately by tracking the position changes. The positions of the vehicle as it drives in a circle is illustrated in Fig. 3.6.

Due to space constraints, the path could only be a constant 2.7m diameter circle. The vehicle slowly increases its velocity to saturate the tires, until some tire slip is observed. The measured velocity is shown in Fig. 3.7. The blue and green lines indicated the front left and front right encoder measurement respectively, and red line in between indicates the speed measurement from the motor. It can be observed that the gap between the blue and green lines increases, as speed increases. This is expected as the vehicle is travelling in a circle, and the outside wheel (blue) is always faster than the inside wheel (green); this difference increases at higher speeds.

Lateral force is calculated from Equation (2.2), r is obtained from the IMU's yaw rate, $\ddot{y}$ is obtained from the IMU's lateral acceleration measurement. V_x is obtained through the encoder measurement. Longitudinal weight shifting is considered negligible. The front and rear lateral force are calculated based on the weight distribution of the vehicle. This

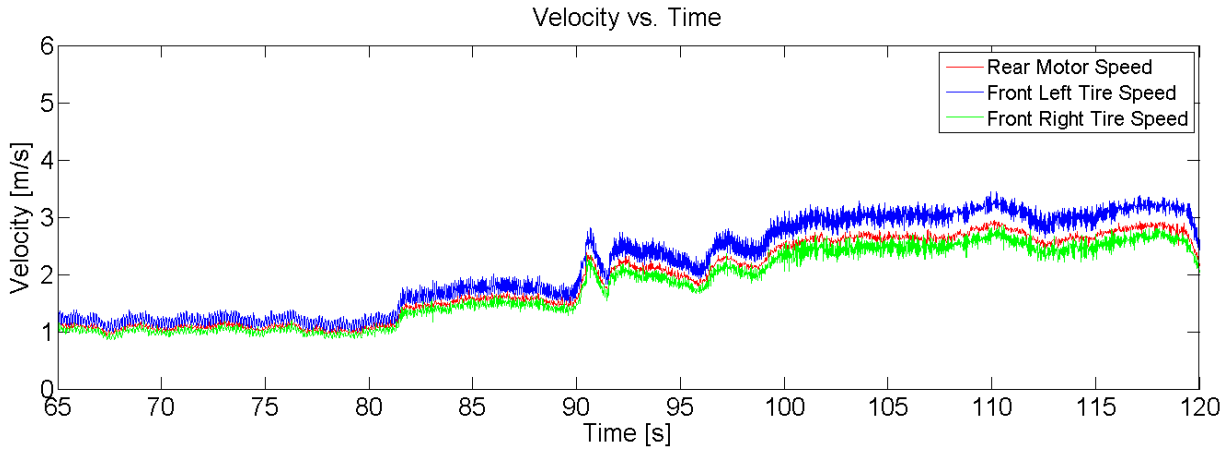

Figure 3.7: Velocity of the test vehicle during tire characterization

assumes that the yaw acceleration is negligible. The testing facility has a uniform concrete floor. The coefficient of friction, μ, is obtained by measuring the amount of force needed to drag the vehicle laterally. While it is known that pneumatic tires can achieve higher than theoretical static coefficient of friction when running, this effect is assumed to be negligible. The coefficient of friction is measured to be constant at 0.65.

The alignment moment is calculated from the current drawn by the steering servo. Prior to the test run, the steering servo is characterized to determine is current vs. torque relationship. The servo is mounted on the table, and weights are incrementally added to the end of the servo arm, while monitoring the current drawn. This curve is shown in Fig. 3.8. The data is fitted to a 2^{nd} order polynomial. It can be observed that the 2^{nd} order polynomial, shown in blue, better fits the data ($R^2 = 0.9$) compared to a linear fit ($R^2 = 0.86$).

The lateral force, F_y is calculated using the Dugoff tire model described in Equation (2.11), and the alignment torque M_z are derived from the current-alignment moment relationship shown in Fig. 3.8. Assuming the mechanical trail t_m is negligible, the pneumatic trail t_p can be calculated based on Eq. (2.15).

The lateral force generated by the tires is shown in Fig. 3.9. It can be observed that from 65s to 90s, the lateral force is at more or less constant 4N. This is because the speed was constant during this time (1 m/s). As the vehicle accelerates to 2.9m/s, the lateral force generated increases to 22N. At higher speed, more lateral force is needed to counter the higher centrifugal force. Furthermore, as seen in Fig. 3.9, the noise of the measurement is higher at higher speed. Due to hardware limitations, the encoders produce higher noise

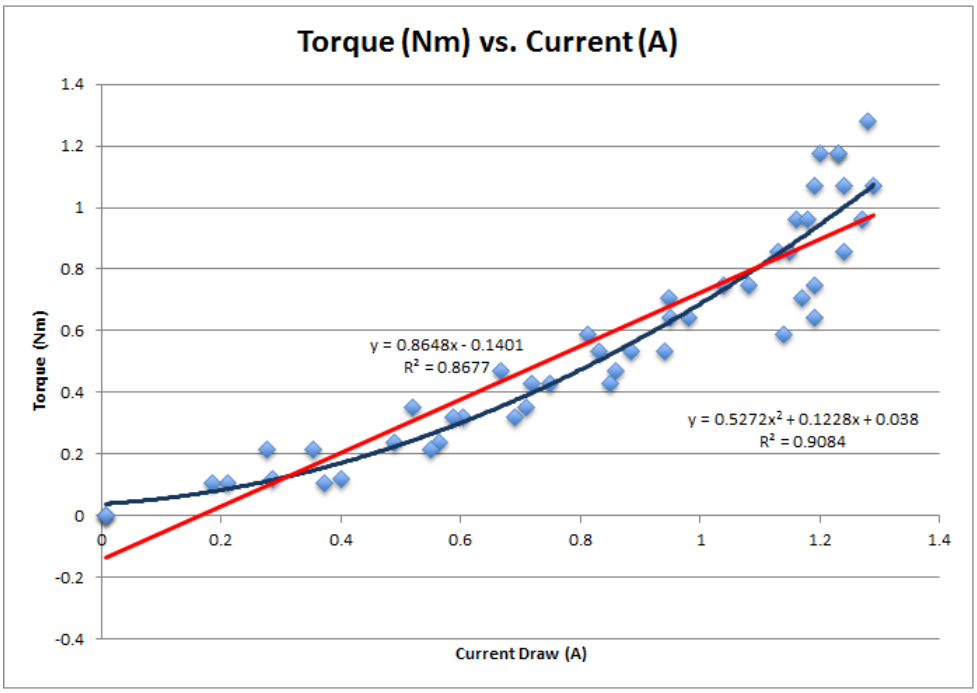

Figure 3.8: Steering torque vs. current

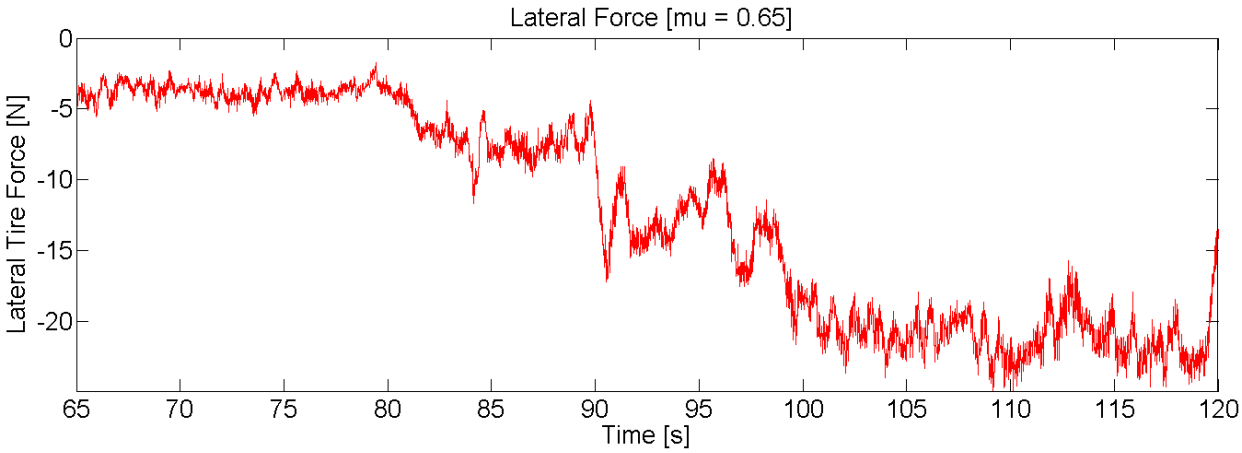

Figure 3.9: Lateral force generated by tires

level at high speed. the noise observed in the lateral force graph is attributed to the encoder noise.

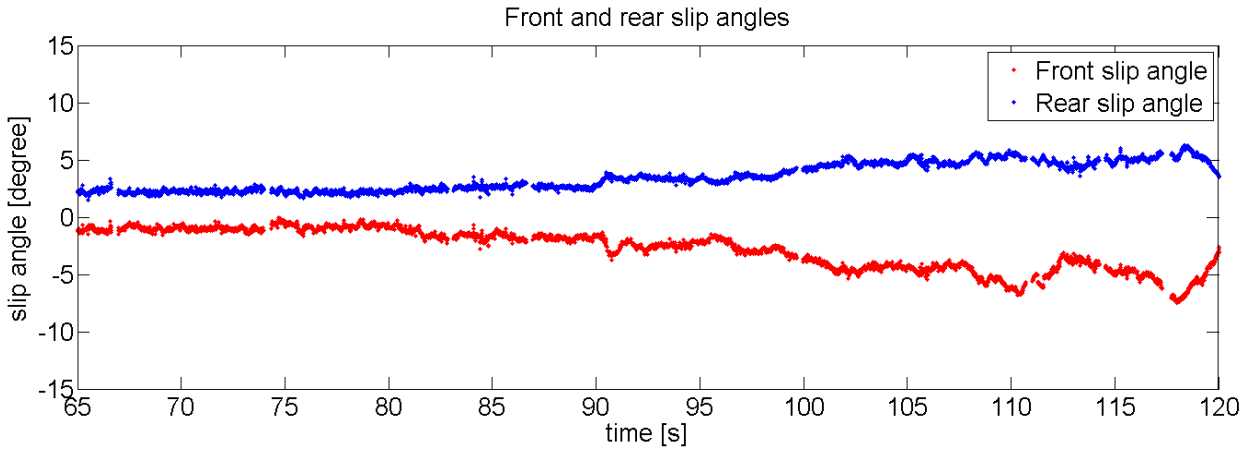

Figure 3.10: Slip angles generated by tires

Slip angles are calculated from measuring the vehicle slip angle β, using the method described in section 3.4. The result is shown in Fig. 3.10. It can be observed that as velocity increases, the magnitude of the slip angles also increases. This is expected; with more lateral force produced, the magnitude of the slip angle should increase. Furthermore, the front and rear slip angles are opposite in signs. This is because the front and rear tires produce lateral forces opposite to each other when the vehicle is travelling in a constant radius circle. In a full side slide, the front and rear tires would produce lateral forces in the same direction. Lastly, the front slip angles, in red, appear to be larger in magnitude compared to the rear slip angle, in blue. When the tires are operating in the linear region, larger slip angles indicate larger lateral force. The unbalanced front and rear lateral forces indicate the yaw acceleration. As the vehicle is accelerating tangentially in a circle, yaw acceleration is introduced, thus causing the unbalanced slip angles.

Plotting the lateral forces and the slip angles, a tire curve plot is obtained, Fig. 3.11. It can be observed that the tire curve obtained is similar to the curve indicated by the Dugoff tire mode. Lateral forces increase linearly with respect to slip angle until 5 degrees. The force generated is then constant. Due to space constraints, the test was stopped before the vehicle tires exceed the maximum tire force; thus, little data in the non-linear region of the tires are obtained. It can also be observed that the rear tire does not seem to have exactly the same slope as the front tires, this can be attributed to three major factors. Firstly, the assumptions made that there is no longitudinal weight transfer may not be accurate. For the higher slip angles, the vehicle was in a state of constant longitudinal acceleration, the rear tires experienced more down force than when the vehicle was travelling at a constant speed. As seen in Fig. 2.3, higher force produces a steeper cornering stiffness. Secondly,

the single track bicycle model assumes only one rear wheel, furthermore, this test assumes that the front and rear tires are exactly the same. This is not the case, as any camber difference, lateral location offset, toe in/out, tire wear could all cause the front and rear tires curves to be different. Lastly the yaw acceleration is assumed to be negligible in the force distribution calculation. Yaw acceleration would indicate that the front slip angles generate more lateral forces than the rear tires. As such, the front tires should have a slightly steeper slope than currently indicated, and the rear tires should have a slightly lower slope. Nevertheless, the data does demonstrate a valid tire curve. On a smooth surface with a friction coefficient of 0.65, the tires have a linear region of approximately 5 deg. The cornering stiffness, C_α, for the linear region is approximately 5N/deg, shown as a green line. Using the lateral forces calculated above and the measured steering torque,

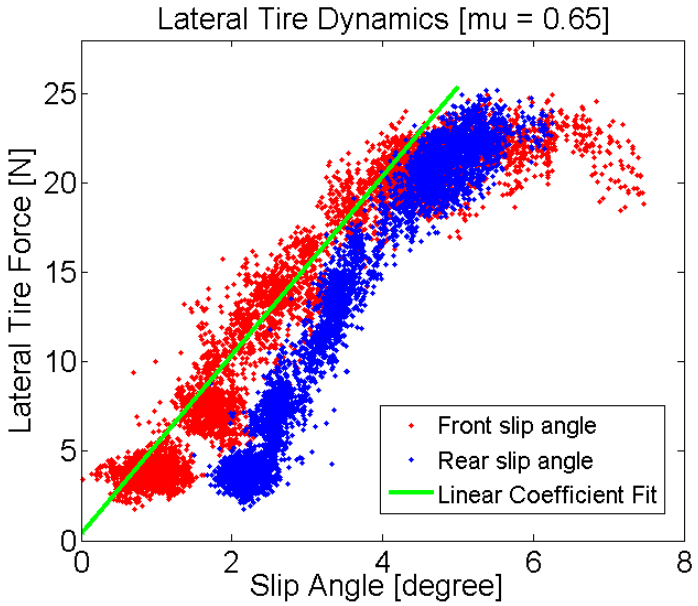

Figure 3.11: Lateral tire dynamics

the pneumatic trail is calculated and shown in Fig. 3.12. The magnitude of the pneumatic trail decreases as tires become more saturated at higher speeds. In the lower slip angle regions, the pneumatic trail appears to be very more noisy. This can be attributed to the alignment moment measurement. Since the alignment moment is measured through the servo current draw, spikes in current would cause spikes in the alignment moment measurement. At lower slip angles, the steering angle requirement is lower, and the inner control loop of the servo produces significant current spikes as the servo is regulated to the

desired angle. As observed from the steering angle data, at higher slip angles, the steering servo reaches at its maximum range, and current drawn is limited by the servo hardware, thus the current draw is more consistent.

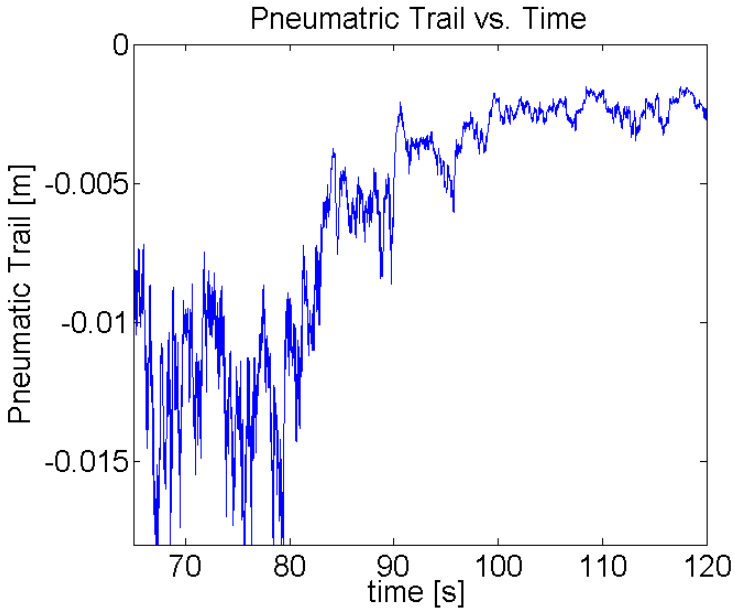

Figure 3.12: Pneumatic trail for the front tires

In conclusion, the small testbed is flexible in its hardware and software setup to accommodate various sensors for testing purposes. The steering servo is selected to be high torque and fast to minimize latency in steering, thus improves the high frequency response of the scale platform. The tires selected are deemed very wide when scaled to a full size vehicle; however, as a testbed to be used for autonomous control at the limit of friction, the increased contact area improves traction, and is positive in helping the vehicle stabilize. The tires are tested in a controlled manner, and the dynamic response of the tire follows that described in the Dugoff model. This response is very similar to full size pneumatic tires, at least in the linear or the near linear regions. The C_α of the tires, at $\mu = 0.65$, is 5N/deg. Lastly, pneumatic trail for the tires are calculated, it was found that the method of measuring torque based on servo current produces a lot of noise due to the servo's internal control loop. This signal should be heavily filtered before use. Alternative method of determining steering torque should also be explored.

Chapter 4

Slip Angle Estimator based on Pneumatic Trail

Autonomous driving at the limits of friction requires accurate estimates of the slip angle throughout the operating envelope. This Chapter presents an observer design that does not rely on expensive sensors. Based on the Dugoff tire model, the observed incorporates pneumatic trail measurements to accurately estimate the tire slip angles. It is validated in both simulation and experiments, and demonstrated improved performance over a larger set of driving conditions.

4.1 Lateral Force and Pneumatic Trail

As the tire saturates, the pneumatic trail approaches zero, and the aligning moment approaches zero [24]. Eq. (4.1) shows a simplified pneumatic trail calculation, derived from the equation presented in [24] and the Dugoff tire model. It is important to note that this model is not accurate for very small small slip angles, or slip angles outside of the slip circle region. However, this equation does account for longitudinal dynamics for slip angles within the slip circle.

$$t_p = \begin{cases} t_{p0} - \dfrac{t_{p0}}{3} I_f |\sqrt{(C_1)^2 + (C_2)^2}|, & \text{if } \sigma \geq 1 \\ 0, & \text{if } \sigma < 1 \end{cases} \tag{4.1}$$

with

$$C_1 = \frac{C_\alpha \tan(\alpha)}{1+\kappa}, ceC_2 = \frac{C_\kappa \kappa}{1+\kappa} \tag{4.2}$$

In Eq. (4.1), the pneumatic trail model begins at an initial trail t_{p0} and decays to zero as the limits of tire adhesion are reached. A reasonable estimate for t_{p0} is assumed to be $\frac{l}{6}$, where l is the length of the tire contact patch[24]. This model ignores the longitudinal effects due to scrub radius, which may contribute up to 4% error [26]. Some assumptions are necessary for the formulation of this equation. [24]

- There are no carcass deformations in the tires
- The tires are isotropic. This implies that unit lateral deformation is equal to the unit longitudinal deformation.
- The tire is operating at steady state, the relaxation length effects and other dynamic effects are not modelled.

4.2 Observer Description

The proposed observer uses a linear observer with the Dugoff tire model to update the slip angles and vehicle dynamics, shown in Fig. 4.1. The inputs, shown in green blocks, are all obtained from inexpensive sensors available on most commercial vehicles. The basis structure is a linear observer based on the Dugoff tire model, shown in blue. It uses wheel speeds, longitudinal, lateral accelerations, and yaw rate to estimate the slip ratio, slip angle and lateral force. This information is then passed onto the pneumatic trail block, where a refined estimation on the inverse peak is output. This output is then fed into the linear observer Since the inverse peak force coefficient is a function of both the friction coefficient and the normal force, this set-up allows precise estimation of slip angle without having accurate knowledge of the normal force or the friction coefficient. This method, however, does require an accurate estimate on the friction coefficient, as well as accurate initial tire parameters.

The observer requires initial values to start. Initially, we assume no longitudinal weight shift in order to calculate F_{zf} and F_{zr} using Eq. (4.3).

$$\begin{aligned} F_{zf} &= \frac{l_r F_{z0}}{L} \\ F_{zr} &= \frac{l_f F_{z0}}{L} \end{aligned} \tag{4.3}$$

Then, we select a nominal coefficient of friction, μ_0, and normal force, F_{z0}. make an initial guess on the front wheel inverse peak force coefficient, I_f based on Eq. (4.11). Assuming

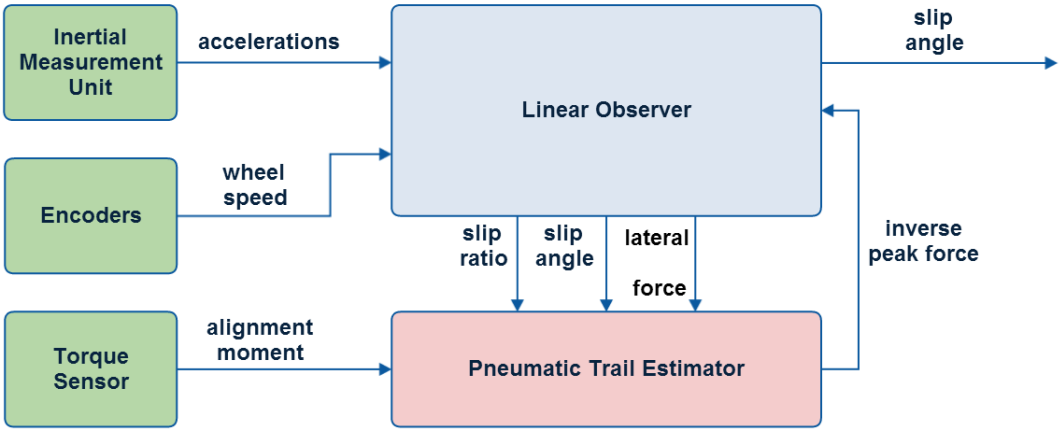

Figure 4.1: Observer block structure

the vehicle starts from standstill, the estimated slip angle, $\hat{\alpha_f}$, can be set to zero. The algorithm then proceeds as follows:

First, the rear tires peak force coefficient, I_r is calculated using Eq. (2.14) and the estimated I_f:

$$I_r = \frac{I_f F_{zf}}{F_{zr}} \tag{4.4}$$

Assuming a front or rear wheel drive vehicle, the longitudinal slip ratio estimate, $\hat{\kappa}_f$ from Eq. (2.9) can be calculated using the front and rear wheel velocity data. For a four wheel drive vehicle, an EKF or other non-linear estimation methods can be used to calculate the tire slip ratios.

With known I_f, $\hat{\kappa}_f$, and $\hat{\alpha}_f$, lateral force, $\hat{F}_{yf}$ can be calculated using the Dugoff tire model presented in Eq. (2.11).

In order to calculate the slip angle at each time step, the change in slip angle is derived using Eq. (2.6). Note that this derivation does not assume a constant V_x, and accounts for the longitudinal dynamics of the vehicle.

$$\dot{\alpha}_f = \dot{\delta} - \dot{\beta} - \frac{l_f \dot{r}}{V_x} + \frac{l_f r \dot{V}_x}{V_x^2} \tag{4.5}$$

where $\dot{\delta}$ is the change in steering angle in a time step, $\dot{\beta}$ is calculated from Equation (2.2); it can be rewritten as the following. The forces, F_{yf} and F_{yr} are obtained from the previous steps.

$$\begin{aligned}\dot{y} &= \frac{(F_{yf} + F_{yr})}{m} - V_x r \\ \dot{\beta} &= \frac{(F_{yf} + F_{yr}) - r}{m V_x}\end{aligned} \tag{4.6}$$

From Eq. (4.5), $\dot{r}$ can be calculated from the single track bicycle model (Eq. (2.2)):

$$\dot{r} = \frac{l_f F_{yf} - l_r F_{yr}}{I_z} \tag{4.7}$$

Therefore, based on Eq. (4.5), the observer update rule can be described as:

$$\dot{\hat{\alpha}}_f = \dot{\delta} - \dot{\beta} - \frac{l_f \dot{r}}{V_x} + \frac{l_f r \dot{V}_x}{V_x^2} + K_o(\hat{F}_{yf} - \tilde{F}_{yf}) \tag{4.8}$$

where K_o is the observer gain, and $\tilde{F}_{yf}$ is given by:

$$\tilde{F}_{yf} = m a_y - \hat{F}_{yr} \tag{4.9}$$

Using the control law derived, an estimate on the slip angle, $\hat{\alpha}_f$, can be obtained by integrating the observer update rule, Eq. (4.8).

using Eq. (2.7), $\hat{\alpha}_r$ can be calculated from $\hat{\alpha}_f$ using Eq. (4.10).

$$\hat{\alpha}_r = \hat{\alpha}_f - \delta + \frac{(l_r - l_f) r}{V_x} \tag{4.10}$$

Using the estimated rear tire force, $\hat{F}_{yf}$, the pneumatic trail estimate, $\hat{t}_p$, can be updated based on the measured aligning moment, M_z, using Eq. (2.15). In this calculation, the mechanical trail, t_m, is assumed to be a constant.

Using the slip angle estimates, $\hat{\alpha}_f$, update I_f by rearranging Eq. (4.1) and substituting in $\hat{t}_p$.

$$I_f = \begin{cases} \dfrac{3(t_{p0} - \hat{t}_p)}{\left|\sqrt{(\hat{C}_1)^2 + (\hat{C}_2)^2}\right|}, & \sigma \geq 1 \\ \dfrac{t_m}{M_z}, & \sigma < 1 \end{cases} \tag{4.11}$$

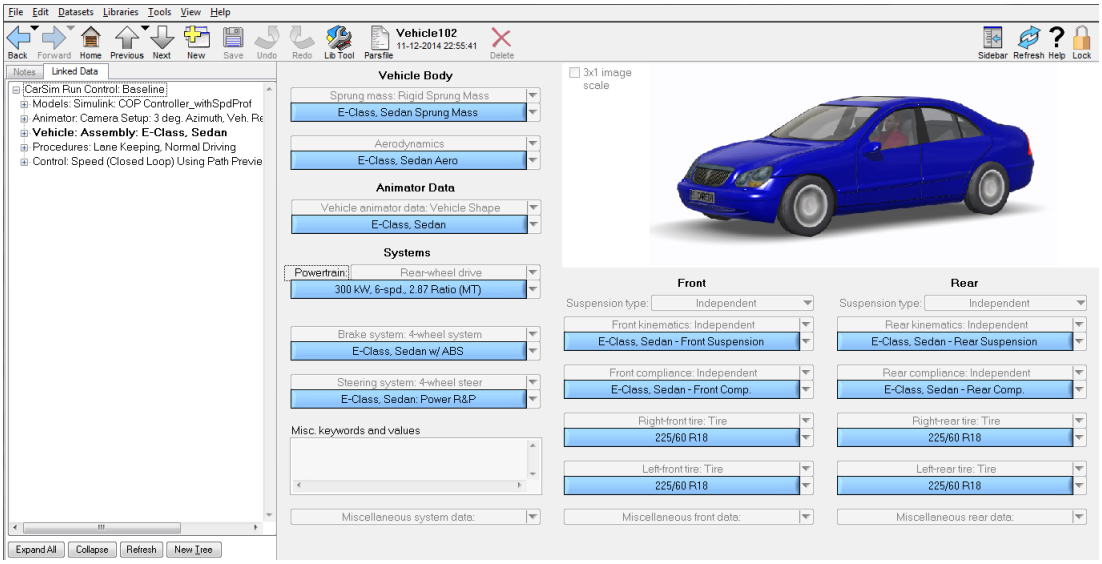

Figure 4.2: CarSim interface

where

$$\hat{C}_1 = \frac{C_{\kappa_f}\hat{\kappa}_f}{1+\kappa_f}$$
$$\hat{C}_2 = \frac{C_{\alpha_f}\tan(\hat{\alpha}_f)}{1+\kappa_f} \tag{4.12}$$

The updated inverse peak force coefficient, I_f can be used instead of the initial guess for further estimations. This process is repeated.

In summary, the algorithm assumes a initial guess on the inverse peak forces and initial slip angles. Tire dynamics are calculated using the Dugoff tire model, and vehicle dynamics is calculated using the single track bicycle model. The tire slip angles are calculated from the vehicle slip angles. The vehicle slip angle update rule is derived based on the bicycle model, making no assumptions on the longitudinal velocity. Lastly, a pneumatic trail observer takes in the force and slip angle estimates as well as the alignment moment measurements, and updates the inverse peak force.

4.3 Simulation Tests Set-up

The observer is verified using a high fidelity vehicle model in CarSim, the interface is shown in Fig. 4.2. CarSim is developed by the University of Michigan Transportation

Research Institute (UMTRI) in the 1980s to create new vehicle models with unparalleled computational efficiency. The tire models in CarSim are created based on [5] and [24]. The vehicle model captures the vehicle dynamics such as longitudinal and lateral dynamics, aerodynamics effects, steering and wheel geometry etc. The tire model used is derived from empirical test data. The vehicle parameters are listed in Table 4.1.

Table 4.1: Vehicle parameters

Vehicle Parameters	**Value**
m	1650 kg
l_f	1.4 m
l_r	1.65 m
I_z	3234 kgm^2
C_α	89000 N/rad
C_κ	75000 N
μ	0.7

Random Gaussian noise is added to each sensor measurement. The sensors and the estimation loop both update at 100 Hz with the following noise variances:

Table 4.2: Sensor frequency and noise parameters

Sensor	**Frequency(Hz)**	**Standard Deviation**
Encoders	100	1.2 m/s
IMU- acceleration	100	2.25 m/s/s
IMU- yaw rate	100	2 deg/s
Torque sensor	100	2.25 Nm

Three estimation techniques are compared in the following simulation:

LL: Linear observer with longitudinal dynamics.

LP: Linear observer with lateral dynamics and pneumatic trail estimation, as implemented in[15].

LLP: Linear observer with longitudinal dynamics and pneumatic trail estimation method presented in this thesis.

The performance of the three estimation techniques is compared in the following test scenarios: constant steering with delayed constant longitudinal acceleration, slalom steering with delayed constant longitudinal acceleration, and ramp steering with delayed constant longitudinal acceleration.

The constant steering test is used as a baseline to compare the observers' performance in both low and high longitudinal dynamics driving scenarios. In this test, the vehicle steering angle is maintained at a constant 3 degrees. From 0s to 40s, the vehicle accelerates to 20km/h and maintains this speed. From 40s to 110s, the vehicle accelerates at a maximum rate of 10km/h/s.

The slalom test is useful in judging observers' performance in extreme driving scenarios. In this test, the vehicle steering angle oscillates in a sine wave with an amplitude of 5 degrees and frequency of 0.35 rad. Similar to the constant steering test, the vehicle initially accelerates to 20km/h and maintains this speed for 40 seconds; it then accelerates longitudinally at a maximum of 5km/h/s for 50s.

The ramp steering test is used to compare the performance of the three observers in scenarios with prolonged operations at the limit of tire stability. For the first 15 seconds of the test, the vehicle maintains a 4.5 degrees steering angle. For the next 35 seconds, the vehicle increases its steering angle at 0.5 degrees/s until its maximum steering angle. The longitudinal input is identical to that in the slalom test.

4.4 Simulation Results and Discussions

4.4.1 Constant Steering Test

In the constant steering test, shown in Fig. 4.3, two observations can be made. Firstly, the velocity measurement is realistic in simulating the sensor noise. Furthermore, the small periodic spikes in the longitudinal slip ratio are due to gear changes. The oscillatory vehicle response in the second half of the test indicates significant tire slip. This is when the tires are fully saturated, and even little disturbances would result in significant tire slip. When lateral tire slip is too large, the tires cannot generate enough longitudinal force, and the vehicle is forced to reduce speed, and the tires regain traction, and reducing the slip angles. This process is repeated, resulting in the large oscillatory motion shown in graph.

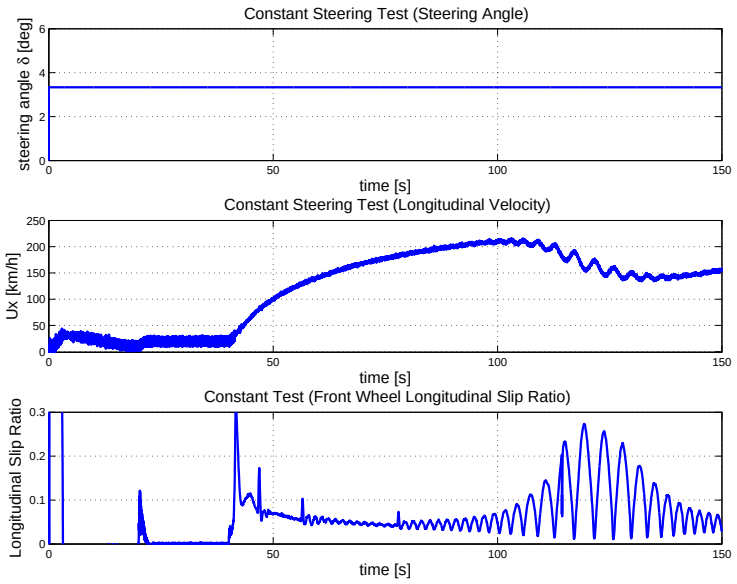

Figure 4.3: Constant steering manoeuvre

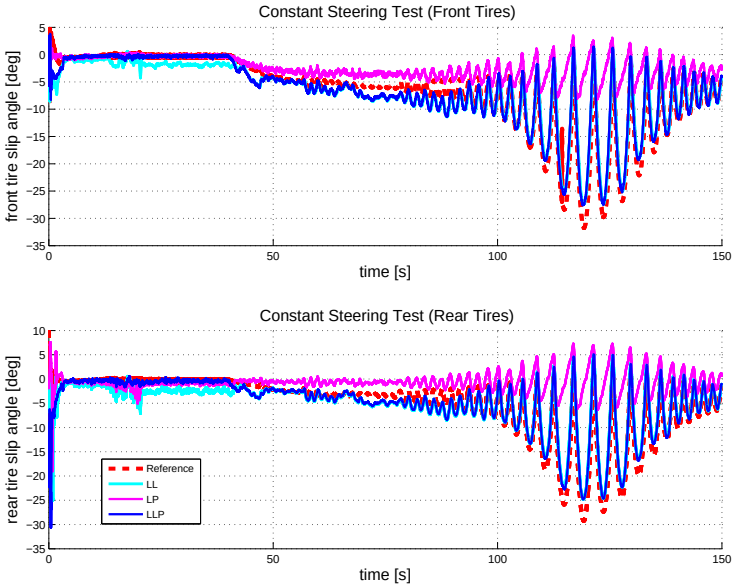

Figure 4.4: Constant steering test results

In Fig. 4.4, from t = 0s to 40s, the longitudinal dynamics are not significant; $\kappa \approx 0$. During this period, all three estimation methods track slip angles well; however, LL appears

to be more noisy than the other observers. The pneumatic trail blocks in LP and LLP attenuate some of the ill effects of measurement noise.

From t = 50s to 110s, the effects of the longitudinal dynamics become noticeable; $\kappa \approx 0.05$. LP estimates begin to deviate from the actual slip angle measurements. This is because LP does not model longitudinal slip.

From t = 110s to 150s, the front tires are fully saturated, and longitudinal slip become significant as $\kappa \approx 0.1$. LP significantly underestimates the slip angle, but both LL and LLP track the slip angle well into the non-linear region ($\alpha \geq 10$ degrees) with an average errors less than ± 3 degrees.

4.4.2 Slalom Test

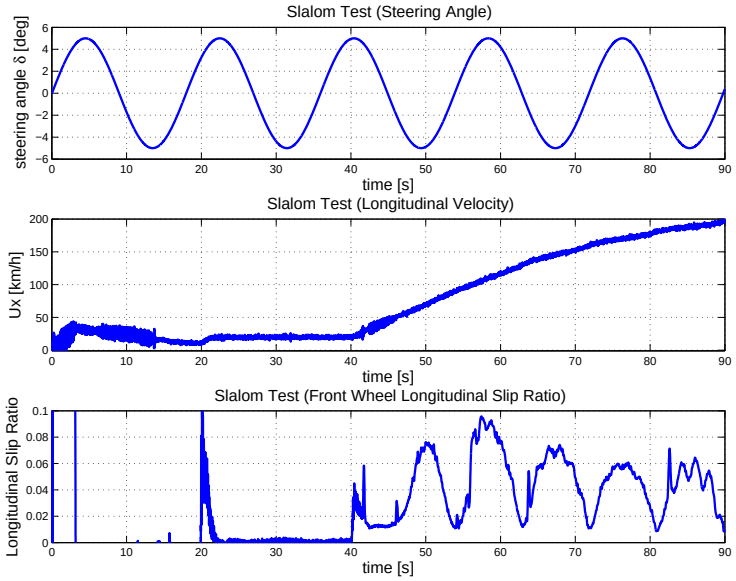

Figure 4.5: Slalom test manoeuvre

In the slalom steering test shown by Fig. 4.5 and Fig. 4.6, similar observations to the constant steering test can be made, with the following additions: From t = 0s to 5s, LL produces a noticeable amount of noise and bias in the linear region, especially when the vehicle is shifting gear. Nonetheless, LLP is able to adapt to the gear change, and track the actual slip angle with an average error smaller than 1 degree. From t = 40s to 90s, LLP is able to track the slip angle in the non-linear region, whereas LP plateaus when high longitudinal slip is present.

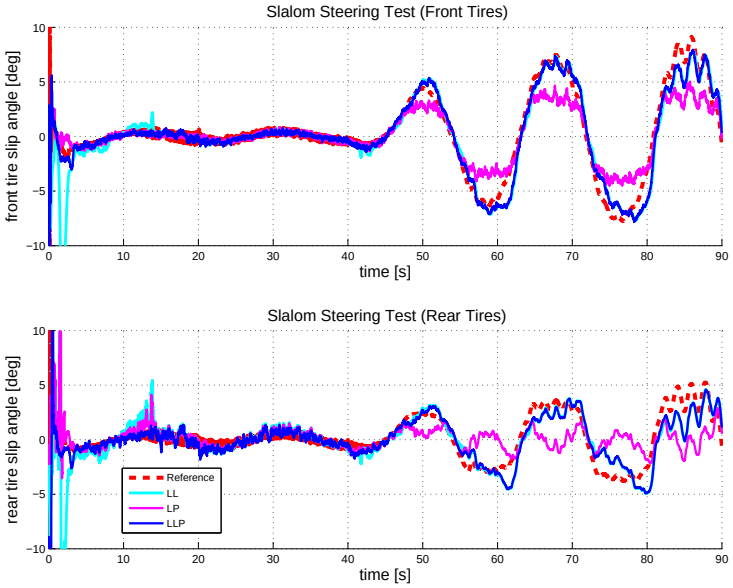

Figure 4.6: Slalom simulation results

4.4.3 Ramp Steering Test

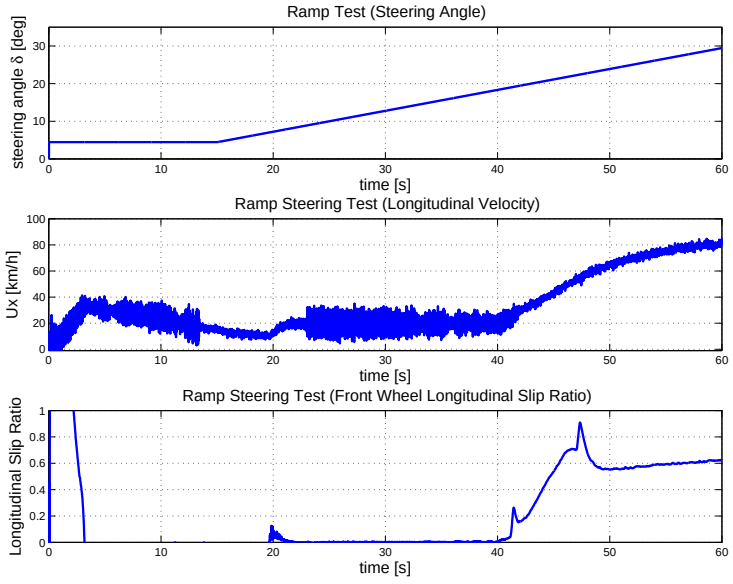

Figure 4.7: Ramp test manoeuvre

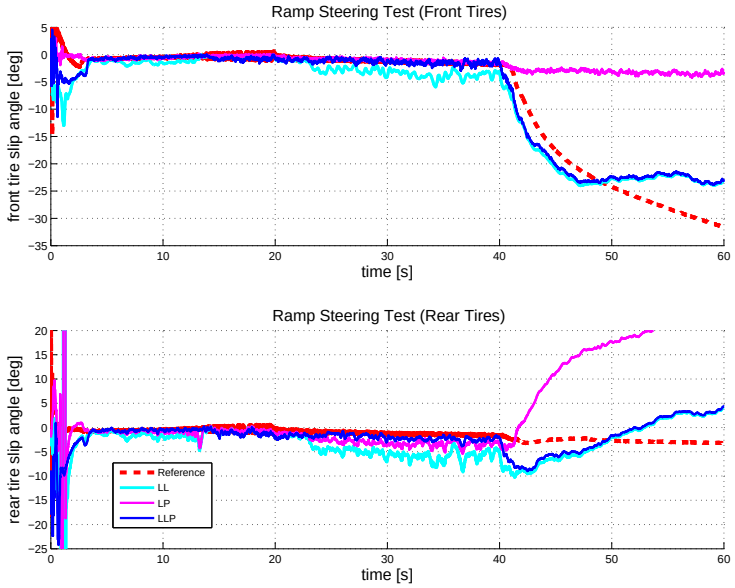

Figure 4.8: Ramp test simulation results

In the ramp steering test, Fig. 4.7 and Fig. 4.8, similar observations can be made to the above two experiments, with the following addition: From t = 50s to 60s, the tires are fully slipping; $\kappa \geq 1$, all three observers fail to estimate the slip angle. When tires are completely saturated, higher order dynamics, such as carcass deformation and lateral force transfer, become significant. These unmodelled dynamics ultimately lead to failed estimation.

4.4.4 Discussions

In the non-linear region, LP's estimates on the magnitude of the front tire slip angle is significantly lower than the actual. This is due to the ignored longitudinal effects saturating the total available force. As a result of the underestimated front slip angles, the rear tire slip estimation is overestimated to account for the vehicle accelerations. With better estimated front tire slip angle, in the case of LL and LLP, the rear tire estimation error is reduced.

Figures 4.4, 4.6, 4.8 demonstrate that the LLP method tracks the actual slip angle well in both linear and non-linear slip regions; in most cases, LLP outperforms both LL and LP. This is noted by comparing the average variances between the three methods, shown in Tables 4.3 and 4.5.

Table 4.3: Average error variance of front slip angle: const. speed (0s - 40s)

Estimator	**Const. Steering**	**Slalom**	**Ramp Steering**
LL	4.48	3.82	2.28
LP	0.48	0.48	0.08
LLP	1.94	1.01	0.16

Table 4.4: Average error variance of rear slip angle: const. speed (0s - 40s)

Estimator	**Const. Steering**	**Slalom**	**Ramp Steering**
LL	8.56	4.80	8.48
LP	3.70	2.36	1.94
LLP	7.56	3.67	0.63

From Tables 4.3 to 4.6, it can be observed that with no significant longitudinal acceleration present, LP tracks the actual slip angle with the smallest error; while LL tracks the slip angle with larger errors. With pneumatic trail information incorporated, the tracking variance is reduced, as shown in the error variance of LLP.

When accelerating, LP does not track the slip angle accurately, showing 20 times worse error than LL and LP at times. LL is able to track the slip angle more consistently, achieving 2 to 20 degrees of standard deviation. LLP exhibits most accurate tracking with the lowest error variance, even in situations with longitudinal dynamic present, or when tires are saturating.

The above simulations demonstrated that the observer design presented in this paper, LLP, is able to achieve accurate estimation near the centre of slip circle, where low longitudinal and lateral dynamics are present. Through the slalom and the ramping test, it is shown that the observer can also estimate the slip angles well near the edge of the slip angle, where significant longitudinal dynamics are present, to the point where friction limit is reached.

The proposed observer integrates a linear observer with Dugoff tire model and a pneumatic trail estimator. This design is fast to operate, and does not require expensive sensors. It uses pneumatic trail to accurately estimate the slip angle in the non-slip region. Using

Table 4.5: Average error variance of front tire slip angle: accelerating (40s+)

Estimator	Const. Steering	Slalom	Ramp Steering
LL	3.73	1.50	22.14
LP	75.12	4.43	409.65
LLP	3.68	1.17	21.32

Table 4.6: Average variance of the rear tire slip angle in the accelerating region (40s+)

Estimator	Const. Steering	Slalom	Ramp Steering
LL	3.86	1.52	21.50
LP	78.31	5.86	377.99
LLP	3.49	1.41	18.61

the Dugoff tire model, it is also able to accurately track the slip angle into the slip region of the tire, even with a significant amount of longitudinal dynamics present. As verified by the three simulated test scenarios, this observer design consistently outperforms other common observer designs.

4.5 Experimental Results and Discussions

The vehicle testbed described in Chapter 3 is used to experimentally verify the estimator's performance. Please refer to Table 4.1 for the test vehicle parameters. As noted in Chapter 3, the tires are stiffer compared to full scale tires, and the steering currents are noisy in the lower slip angle region. Data collected from the test to characterize the tire model are passed through an running average filter. The path is a circle with a constant radius, and the vehicle accelerates along this path until slip is noticed, the velocity profile is shown in Fig. 3.7 in Chapter 3. Due to space constraints, the experiment does not push the vehicle pass the limit of friction. The space only allowed clearance to track a circle with a diameter of 2.7 m. The theoretical maximum speed before tire saturation for this condition is 2.9 m/s, which is the maximum vehicle speed observed, as shown in Fig. 3.7.

The slip angles generated from the test are shown in Fig. 4.9. The blue and red lines indicate respectively the front and rear slip angle estimates from the proposed estimator (LLP). As a comparison, the results from a linear observer using the Dugoff tire model (LL) are shown in pink and black. The true slip angles, as measured from the IPS is shown in cyan and green.

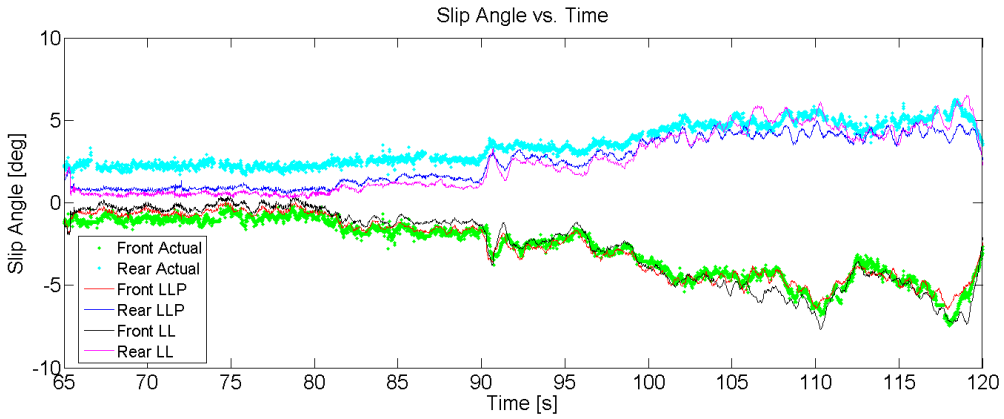

Figure 4.9: Slip angle results from the pneumatic trail estimator

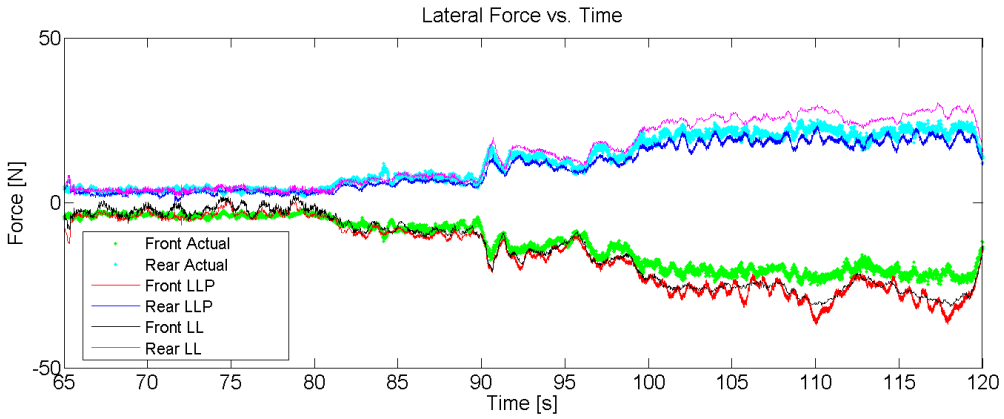

Figure 4.10: Lateral force estimates from the pneumatic trail estimator

It can be observed that the proposed slip angle estimator has a slightly better tracking performance compared to the linear observer. However, both observers seem to follow the trend of the actual slip angle. This could be attributed to two factors. Firstly, it can be noted that the tires was mainly operating in its linear region (slip angle is smaller than 5 deg) during the test. The pneumatic trail observer piece does not have significant

impact on the estimate until the tires are nearly fully saturated. Near tire saturation, the slip angles from the propose estimation shows slightly better tracking with less noise compared to the linear observer itself. Secondly, due to servo current, shown in Fig. 3.12 in Chapter 3, the pneumatic trail information gathered are very noisy, this could contribute to the noisy estimator results. The lateral force estimates from the estimators(LLP and LL) are shown in Fig. 4.10. It can be observed that both the linear observer (LL) and the proposed estimator (LLP) closely track the lateral force exerted. Near the non-linear region, the proposed estimator showed slightly better tracking for the rear tires. This can also be attributed to the two reasons listed above. Due to test facility space restrictions, the vehicle is only pushed to the maximum speed before tires are fully saturated. In order to test for the non-linear tracking performance of the estimator, the vehicle should be fitted with RTK GPS and an accurate IMU, so outdoor tests can be performed, where space is not an restriction.

The proposed observer integrates a linear observer with Dugoff tire model and a pneumatic trail estimator. This design is fast to operate, and does not require expensive sensors. Given accurate tire/road parameters, such as cornering stiffness and coefficient of friction, the model is able to accurately estimate the slip angle in the non-slip region using pneumatic trail. Using the Dugoff tire model, it is also able to accurately track the slip angle into the slip region of the tire, even with a significant amount of longitudinal dynamics present. As verified by the three simulated test scenarios, this observer design consistently outperforms other common observer designs. The experimental result is only obtained for constant radius circle test, it shows good tracking performance for the linear region. However, it only slightly improves over the range of operating conditions the test was able to achieve. Furthermore, for the small vehicle with servo actuated steering, using pneumatic trail in the controller is not desirable due to the noise in measurement. In the next Chapter, a controller is developed that does not depend on slip angle estimation, but instead uses tire forces estimates directly to control the vehicle.

Chapter 5

Controlling Near the Limit of Friction

In [17], K. Kritayakirana and J. C. Gerdes introduced the controller used on the Shelley Autonomous vehicle. The controller is able to maintain vehicle stability, while constantly maximizing vehicle performance, i.e. maximizing tire friction usage. With this controller, the Shelley was able to achieve over 120mph autonomous driving, and was able to complete the Pikes Peak circuit. In order to maintain the vehicle at its tire limit, the controller requires accurate knowledge of slip angle. The Shelley vehicle has two mounted RTK GPS [12] that can provide accurate slip angle data in real time. However, these specialized sensors are expensive, and not found on commercial vehicles.

In Chapter 4, a novel estimation approach is introduced that can achieve accurate slip angle estimates even under longitudinal acceleration. Nevertheless, the observer does fail once tire forces are saturated. Furthermore, if the tire parameters are not estimated correctly, the estimator may contain bias in the slip angle estimates. With a combination of these factors, online, accurate slip angle estimation with inexpensive sensors is very difficult to achieve. For a controller that operates near the tire friction limits, underestimated slip angles may lead the controller to overreact, causing instability and loss of control. In particular, for the small scaled test platform, sensor noises may be more significant, such as the case of pneumatic trail measurement. This motivates a need for a controller design that does not use online slip angle estimates.

An alternative to using slip angle estimation, is using the lateral forces to judge tire dynamics. In this thesis, a controller structure that pushes vehicle performance to the limit of friction without using slip angles estimates is proposed.

5.1 Controller Description

The vehicle controller consists of four sections: speed profiler, lateral controller, longitudinal controller, and a traction control, shown in Fig. 5.1. The speed profiler calculates desired velocities based on the path characteristics a certain distance ahead. The lateral controller uses a full state feedback scheme to reduce the vehicle's heading error and lateral error. The concept of Centre of Percussion (COP) is used as reference point to introduce some stability when tires are slipping. The longitudinal controller monitors the lateral force required, and uses the spare forces to maximize longitudinal performance. On most vehicles, a traction controller is a standard equipment; it monitors differences in the wheels' spins to predict slip, and distribute longitudinal power to counter/minimize the slippage.

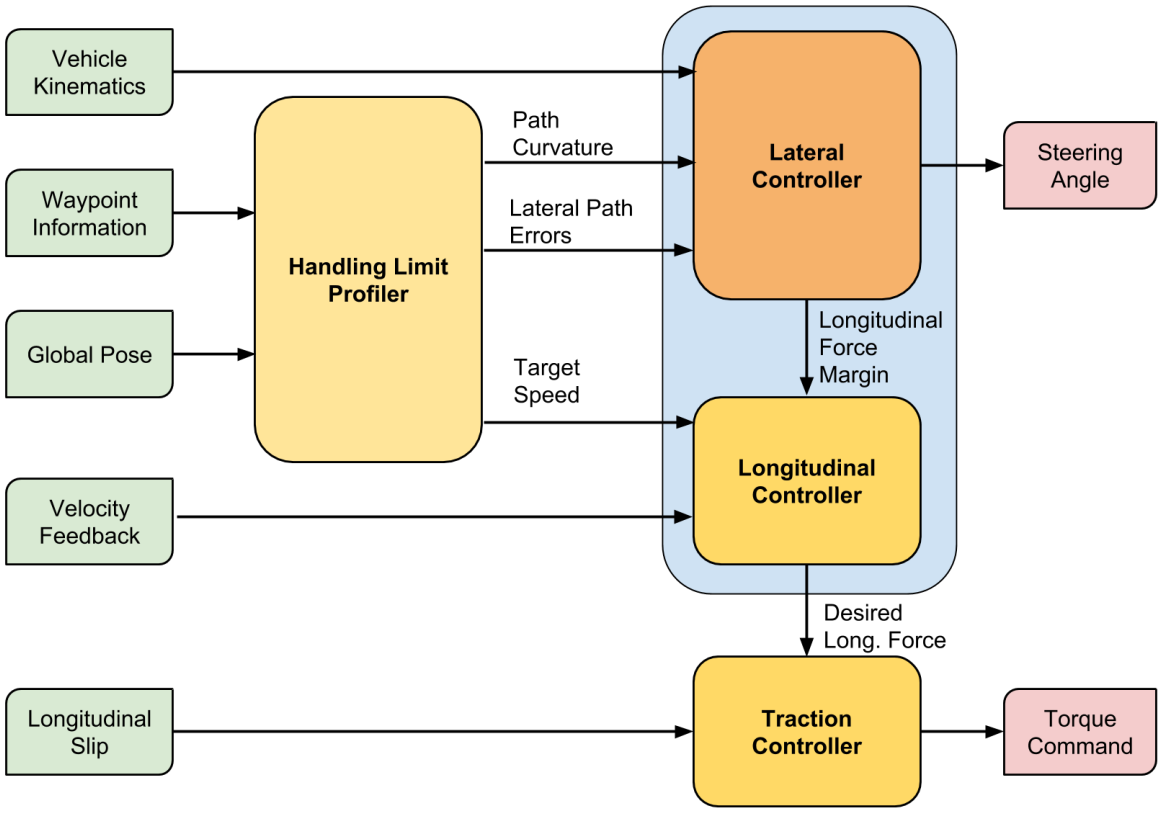

Figure 5.1: Controller architecture

Many methods can be used to generate a speed profile for the vehicle. For racing

purposes, the desires paths are generated offline to optimize vehicle performance. Similar characteristics can be achieved with a sophisticated path planning algorithm. For real-time path planners, a spline method can be used to calculate the desired velocity. The paths ahead of the vehicle is fitted through a high order piece wise spline; the curvatures of each piece is compared; and a velocity profile can be generated for each splines using Eq. (5.1). For the purpose of controller design, the simplest case is used for verifications only. A constant curvature is fit of three points ahead of the vehicle. Using the vehicle coordinates, the lateral distances between the path and three specified points ahead (0m, 5m, and 30m)of the vehicle are found. A circle is fit through the three points; depending on the lateral errors, the radius of the circle changes. This radius is used to calculate a reference velocity based on the centrifugal force and the maximum frictional force supported by the tires.

$$\begin{aligned} F_t &= \frac{\mu l_r m g}{L} \\ F_c &= m\frac{V_d^2}{R} \\ V_d &= \sqrt{\frac{\mu l_r g R}{L}} \end{aligned} \tag{5.1}$$

where F_t is the maximum available tire force, μ is the coefficient of friction, F_c is the centrifugal force generated around a circle with radius R at the desired velocity V_d.

This is a relatively simple speed profiler with several limitations: Firstly, the diameter of the circle can only be as small as the distance between the first and the third points; in this case 30m. This can lead to misses in sharp turns. Secondly, the speed profile assumes that the vehicle will travel along a constant radius curvature, this is usually not the case. Thirdly, in the cases of a sharp U-turn, the speed profile may fail to give a valid answer. This speed profiler, however, is fast to operate and easy to understand. For certain tracks, the circle radius can be optimized by adjusting the look ahead distance. This simple speed profiler does prove useful in many cases where the speed profile is not known.

The lateral controller consists of a feedforward controller and a feedback controller. The feedforward controller uses the centre of percussion of the rear tires, shown in Fig. 5.2 in Chapter 1, to simplify calculations. The centre of percussion with respect to the rear tires is a special point where the sum of lateral acceleration from the rear tire, a_y, is zero. The rear tires produce two effects on the vehicle system. They create a lateral acceleration on the CG, and they produce an angular acceleration about CG. At the COP, these two effects cancel out, and the a_y from the rear tires is zero [17]. Discussed in more depth

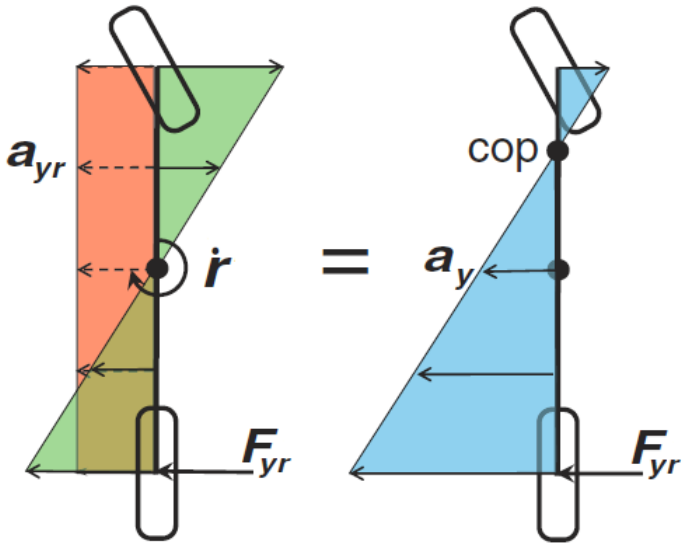

Figure 5.2: Description on COP controller. [17]

in [18], using the centre of percussion as the error reference point has the advantages of simplifying calculations, and improved stability for when the vehicle is operating near the limit of friction. This research also proved that using the COP as a reference point, the vehicle remains stable even when rear tires are highly saturated.

The feedforward controller takes in current path curvature, path distance and velocity, and calculate the forces needed to go through a curve. As described in [18], the feedforward force can be derived below:

$$\begin{aligned} e_p &= e + x_p \sin \Delta\psi \\ \dot{e} &= \dot{y}\cos(\Delta\psi) + V_x \sin(\Delta\psi) \\ \dot{s} &= \dot{y}\cos(\Delta\psi) - V_x \sin(\Delta\psi), \end{aligned} \tag{5.2}$$

where e_p is the lateral error a fixed distance, x_p, away from the CG. $\Delta\psi$ is the heading error. V_x is the vehicle longitudinal velocity, and s is the distance travelled by the vehicle.

Assuming that $V_x\Delta\psi \approx 0$, using a small angle assumption, the following can be obtained:

$$\begin{aligned} \dot{e}_p &= \dot{e} + x_p\Delta r \\ \ddot{e}_p &= \ddot{y} + V_x r - V_x K\dot{s} + x_p\dot{r} - x_p(K\ddot{s} + \dot{K}\dot{s}) \end{aligned} \tag{5.3}$$

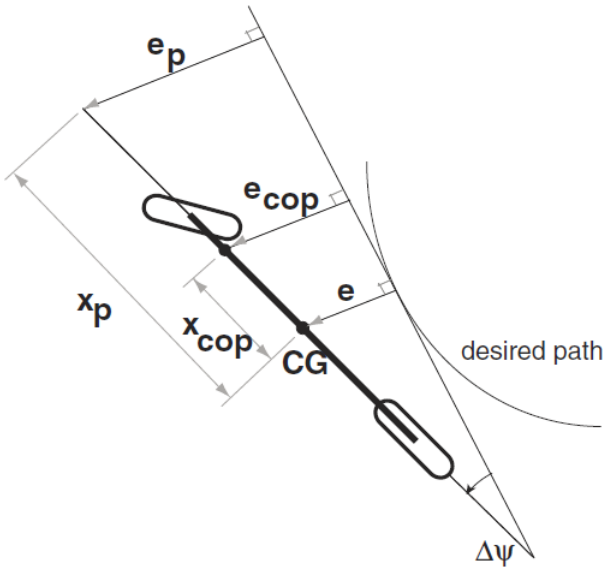

Figure 5.3: Trajectory parameters [18]

where $\ddot{y}$ is the lateral acceleration of the vehicle in vehicle coordinate frame. r is the vehicle yaw rate, K is the instantaneous curvature of the path, and $\dot{K}$ is the change in curvature.

Substitute in the Single Track Vehicle Model from Eq. (2.2) in Chapter 2, the following error dynamic can be written:

$$\ddot{e}_p = \frac{F_{yf} + F_{yr}}{m} + V_x r - V_x K \dot{s} + x_p \frac{l_f F_{yf} - l_r F_{yr}}{I_z} - x_p(K\ddot{s} + \dot{K}\dot{s}) \tag{5.4}$$

Using the concept of centre of percussion, described by Eq. (5.5), the error dynamics can be simplified.

$$x_{cop} = \frac{I_z}{l_r m} \tag{5.5}$$

At the COP, the effect of rear tire forces cancel each other out:

$$\frac{F_{yr}}{m} - x_{cop} \frac{l_r F_{yr}}{I_z} = 0 \tag{5.6}$$

Thus, at the centre of percussion, the error dynamics described by Eq. (5.4) becomes:

$$\ddot{e}_{cop} = \frac{L F_{yf}}{l_r m} - V_x \dot{K} \dot{s} - x_{cop}(K\ddot{s} + \dot{K}\dot{s}) \tag{5.7}$$

The feedforward command is intended to reduce the error dynamics to zero; therefore, the feedforward law is obtained by equating $\ddot{e}_{cop}$ in Eq. (5.7) to zero. The lateral feedforward force, F_{fw} is defined as:

$$F_{fw} = \frac{ml_r}{L}((V_x K\dot{s}) + x_{cop}(K\ddot{s} + \dot{K}\dot{s})) \tag{5.8}$$

The lateral feedback controller uses a simple full state feedback structure. It contains six states: $[e_{cop}, \Delta\psi, \dot{e}_{cop}, \Delta\dot{\psi}, e_p, \Delta\psi_p]$, where e_{cop} is the lateral error at the centre of percussion, $\Delta\psi$ is the current heading error, e_p is the lateral error a fixed distance away, and $\Delta\psi_p$ is the heading error a fixed distance from the vehicle.

The first four feedback states are purely for lane keeping purposes. When regulated to zero, the vehicle will be tracking the path in the correct heading. The last two terms act as a future feedback term. These terms aim to start steering early when a curve is coming up. Much like the human driving behaviour, when a curve is coming up, one would steer slightly in the direction of the curve, thus reducing the amount of steering needed otherwise. The two future terms act like a damper on the original feedback system.

The overall feedback law is described below:

$$F_{fb0} = -k_1 e_{cop} - k_2\Delta\psi - k_3\dot{e}_{cop} - k_4\Delta\dot{\psi} - k_5 e_p - k_6\Delta\psi_p \tag{5.9}$$

where $k_i, i = 1-6$ are the gains for the system.

Practically, there is a limitation on how much force can be exerted by the front tires, the sum of the feedback and the feedforward force should not exceed this amount. Based on the concept of slip circle, the limit is proportional to the friction coefficient of the road. Therefore, the maximum feedback force allowed is limited to the following:

$$\bar{F} = \sqrt{\left(\frac{\mu mgl_r}{L}\right)^2 - F_{fw}^2} \tag{5.10}$$

It should be noted that in this setup, the feedforward command takes priority, feedback force ensures that the vehicle is always operating near the limit of friction. With the limit set, the actual feedback amount is described below:

$$F_{fb} = \max(\min(F_{fb0}, \bar{F}), -\bar{F}) \tag{5.11}$$

The total lateral force is then

$$F_y = F_{fb} + F_{fw} \tag{5.12}$$

Assuming a linear tire model described in Eq. (2.10) in Chapter 2. The slip angle required can be calculated based on an estimated cornering stiffness:

$$\alpha = \frac{F_y}{C_\alpha} \tag{5.13}$$

Making the small angle assumption, steering angle can be calculated from the vehicle side slip angle calculation, Eq. (2.5).

$$\delta = \frac{\dot{y} + l_f r}{V_x} + \alpha \tag{5.14}$$

The last task of the lateral controller is that it needs to inform the longitudinal controller how much tire friction is left, F_m, a similar calculation to the $\bar{F}$ is used:

$$F_m = \sqrt{\left(\frac{\mu m g l_r}{L}\right)^2 - F_y^2} \tag{5.15}$$

The longitudinal controller is a small feedback controller that calculates the desired longitudinal force, based on the lateral force required and the desired speed profile.

From the speed profiler described by Equation (5.1), a desired speed, V_d is obtained. This speed is fed back via a proportional controller with linear gain k_{spd}:

$$F_{spd} = k_{spd}(V_d - V_x) \tag{5.16}$$

, where F_{spd} is the force generated from the desired speed. This force is then compared to the F_m value calculated in Eq. (5.15), the minimum of the two is selected as the longitudinal output.

$$F_x = \min(F_{spd}, F_m) \tag{5.17}$$

When the gains are tuned correctly, simulation has shown that this simple structure is able to maintain the vehicle near its tire frictions on most paths. F_m ensures that the vehicle is always going as fast as it can; however, in situations where a sharp curve appears right after a straight long path, the vehicle would not slow down until it reaches the end of the path. F_{spd} ensures that the vehicle slows down to an acceptable speed that can travel through the turn, before reaching the turn itself.

The last piece in the longitudinal control aspect is a traction controller. The traction controller monitors the longitudinal slip ratio, and ensures that the desired torque at the wheel is reached through a proportional controller.

Furthermore, it ensures that the longitudinal slip ratio does not exceed a dangerous level, in this case, 0.7. The controller would ramp down the acceleration needed if this threshold is exceeded.

5.2 Controller Test Set-up

Figure 5.4: CarSim animation screenshot

The controller is verified using a high fidelity vehicle model in CarSim, described in Chapter 4. The vehicle model captures the vehicle dynamics such as longitudinal and lateral dynamics, aerodynamics effects, steering and wheel geometry etc. Furthermore, CarSim allows animation of the vehicle control in real time, as shown in Fig. 5.4. This feature allows users to visually inspect the controller design, the following parameters are used for the test vehicle model.

The controller is tested through four scenarios: a large circular track, a small circular track, a double lane change, and a high performance race track.

The large circular track, shown in Fig. 5.5, is a basic test to judge the controller performance at steady state. The track is 100m in radius with a constant surface μ of 0.9.

Table 5.1: Controller test vehicle parameters

Vehicle Parameters	**Value**
m	1650 kg
l_f	1.4 m
l_r	1.65 m
I_z	3234 kgm^2
C_α	57295 N/rad
C_κ	71400 N
μ	0.9

The vehicle should be able to reach steady state speed with a constant lateral error. Due to unmodelled dynamics, the vehicle is expected to have slight drifts, but the controller should be able to correct this behaviour. The small circular track is only 40m in radius,

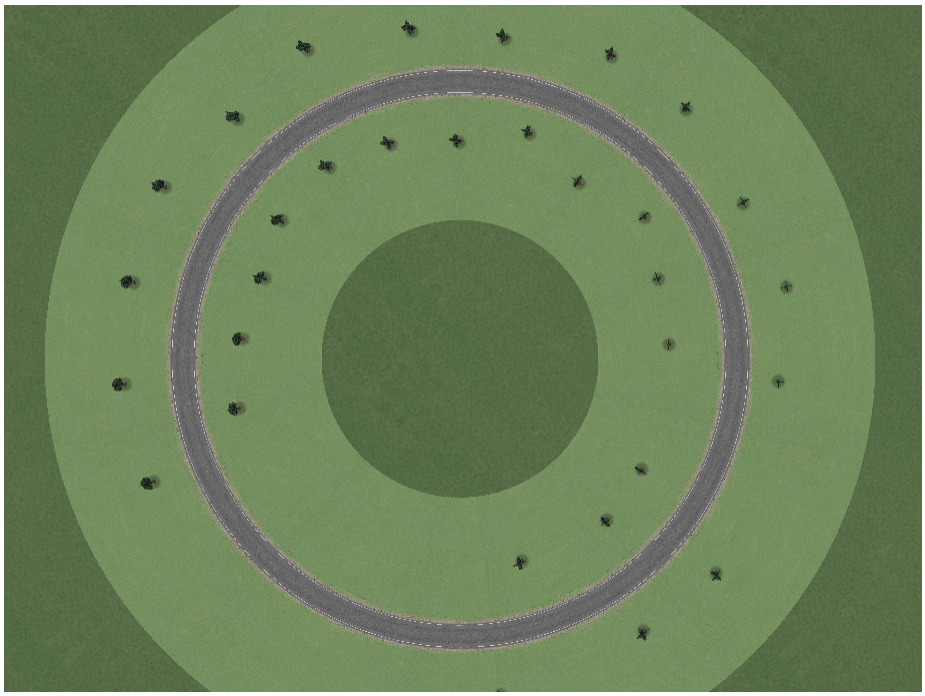

Figure 5.5: Circular track (100m radius)

with a constant surface μ of 0.9. Since the track itself is smaller, the maximum speed achievable should be lower; the steering should also be more aggressive. This test is used to check if the longitudinal controller is decreasing its output when lateral force demand is higher. Similar to the large radius test, drift is expected, but the controller should be able to correct itself.

The double lane change test is an industry standard test. The vehicle is required to quickly change two lanes at high speed to simulate obstacle avoidance on the highway, similar to having a step input to the lateral path. This test aims to test the controller stability, recovery time, overshoot. It is expected that the longitudinal controller will have to brake the vehicle in order to achieve the steering force required. This behaviour would saturate the tires, causing drift and overshoot, but the vehicle should be able to correct itself before control is lost.

The last test scenario is the race track test, presented in Fig. 5.6. This track contains sharp and wide corners, with various elevations and banking angles. This track tests the capability of the controller on a more general course. Since the controller pushes the limit of the vehicle, some drift in the vehicle is expected, especially before a sharp turns. This is an area where the speed profiler should slow down the vehicle before the turn. As a comparison, a PID controlled vehicle is implemented for comparison purposes for the race track.

Figure 5.6: Race track

5.3 Simulation Results and Discussions

5.3.1 Large Circular Track

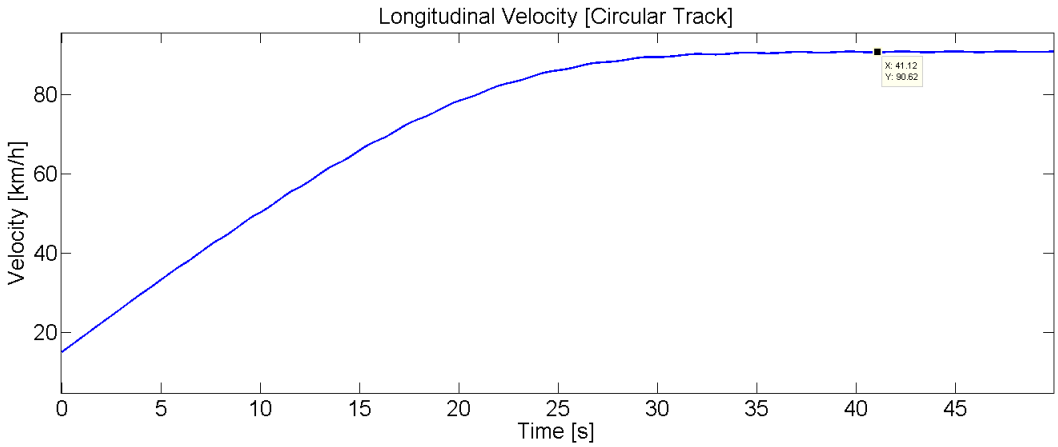

Figure 5.7: Longitudinal velocity for the proposed controller on the large circular track

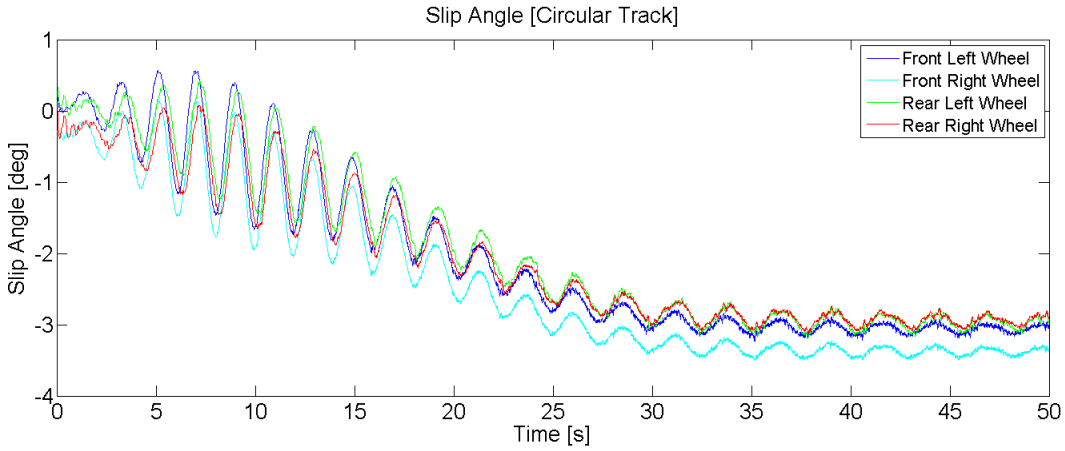

Figure 5.8: Slip angle for the proposed controller on the large circular track

As shown in Fig. 5.7, the car initially started at 15km/h. At this speed, the steering force requirement is not significant, and the longitudinal controller accelerates the vehicle to maximize vehicle performance. At around 32s, the tire forces are nearing their limit, and the longitudinal controller decreases its force output. The vehicle eventually settles at

around 91 km/h. As a reference, the theoretical maximum speed for this track is 106km/h. This effect can be observed in Fig. 5.8, as the vehicle accelerates, the magnitude of the slip angles increases to 3 deg. The lateral errors are measured at the COP. The error

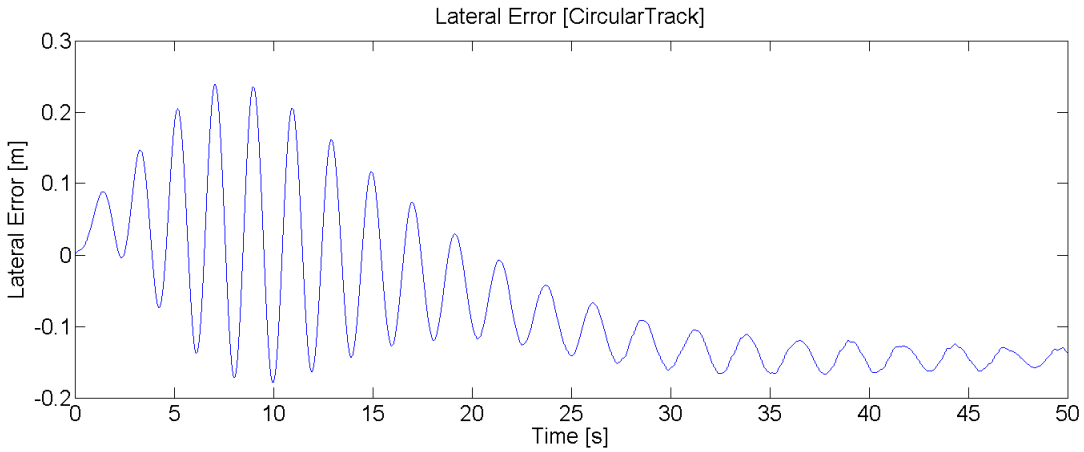

Figure 5.9: Lateral error for the proposed controller on the large circular track

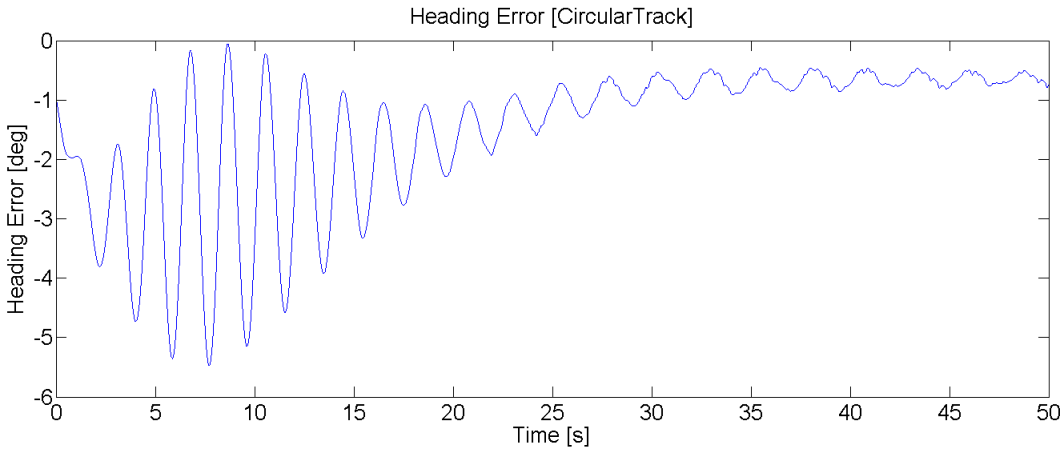

Figure 5.10: Heading error for the proposed controller on the large circular track

starts at 25cm and settles to 15cm. In Fig. 5.10, heading errors are shown to settle to approximately 1 deg after 25s. During accelerations, the controller is trying to balance between the steering effort and longitudinal acceleration. Since the algorithm does not directly monitor slip angles, the tire slips must result in large enough lateral acceleration or lateral error before the lateral controller takes significant action and longitudinal effort

reduces. This struggle is especially pronounced when the tires are operating at the limit of friction, where a little slip could result in large body motion. As the controller loses and regains tire traction, the result is an oscillatory pattern (0s to 25s) observed in the Fig. 5.9 and Fig. 5.10. Once the vehicle reaches steady state, the amplitude of the oscillation also reduces.

5.3.2 Small Circular Track

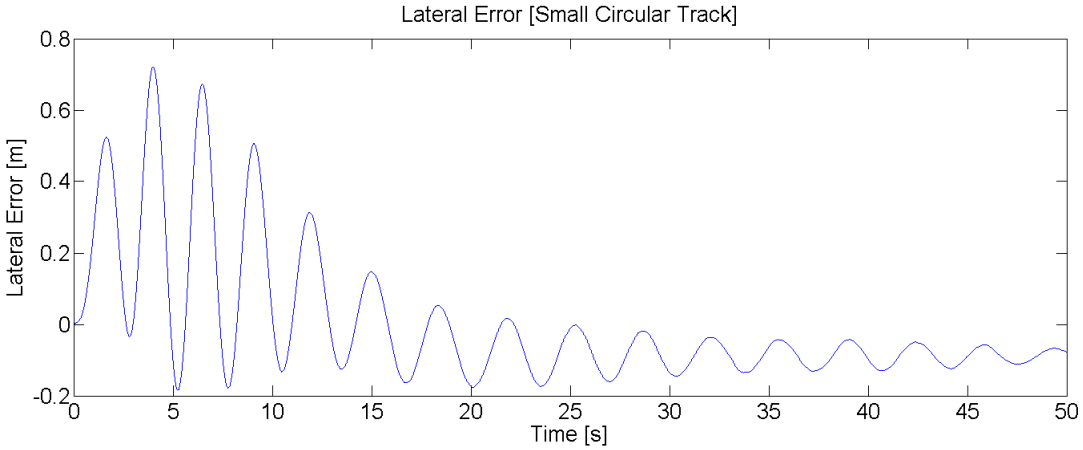

Figure 5.11: Lateral error for the proposed controller on the small circular track

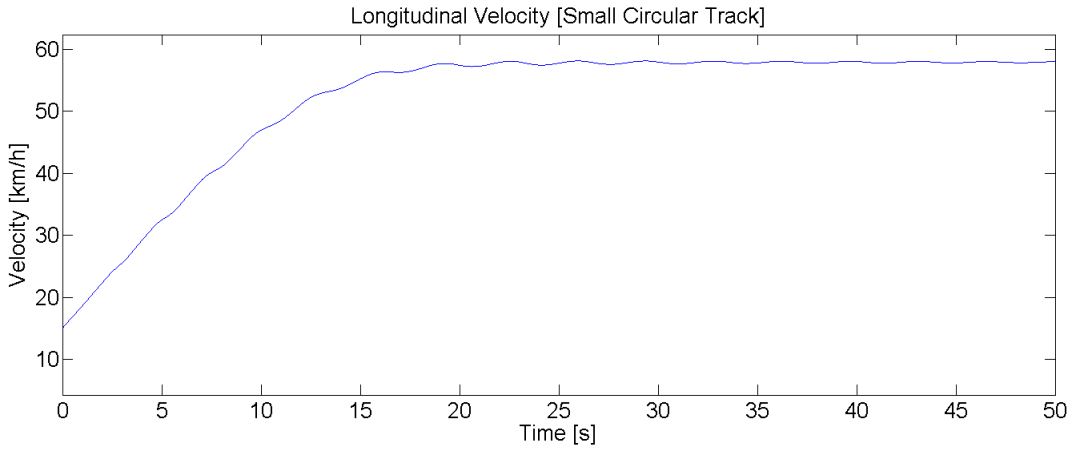

Figure 5.12: Longitudinal velocity for the proposed controller on the small circular track

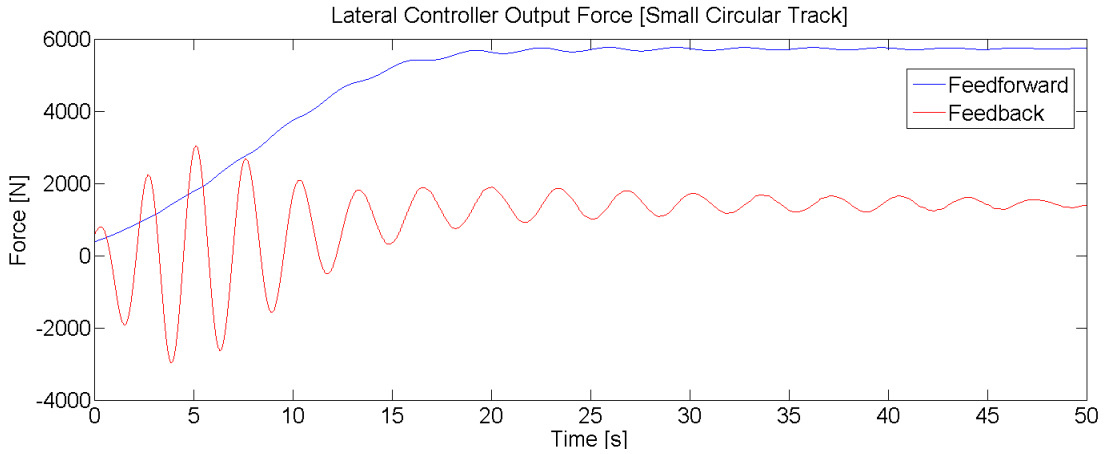

Figure 5.13: Feedforward and feedback forces for the proposed controller

As shown in Fig. 5.12, the small circle test resulted in the settling speed of 60km/h vs. 90 km/h for the large circle test. This is expected, as the smaller radius requires larger steering angles, thus leaving less friction to generate longitudinal force. The composition of feedforward lateral force and the feedback lateral forces are shown in Fig. 5.13. It can be observed that the feedforward forces increase until a wheel begins to saturate. While the feedback controller shows initial oscillation to regulate the steering angle during acceleration; it settles when the steady state speed is reached.

5.3.3 Double Lane Change

The double lane change procedure is performed at 70 km/h. It can be observed from Fig. 5.14 and Fig. 5.15 that the controller is able to handle the sudden change in lateral error well. The vehicle does exhibit some oscillatory motion, especially during the second lane switch. This is because the momentum from the first lane switch has not been completely absorbed by the tires, and the second switch is already required. This quickly saturates the tires, and lead to instability.

Nonetheless the overall errors did not exceed 0.6m; this demonstrates that the controller is able to handle the fast dynamic change as described. It is able to detect when tires are saturated, and take measures against loss of control.

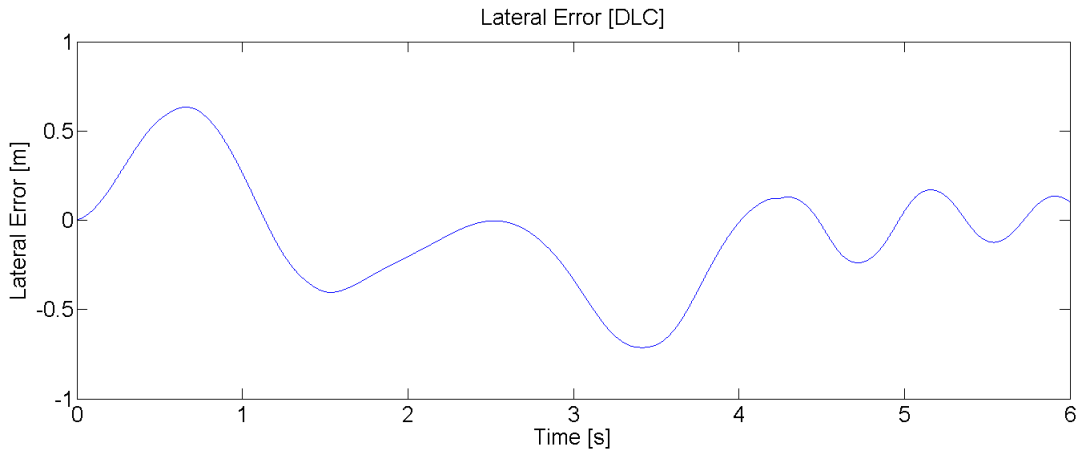

Figure 5.14: Lateral error for the proposed controller during double lane change

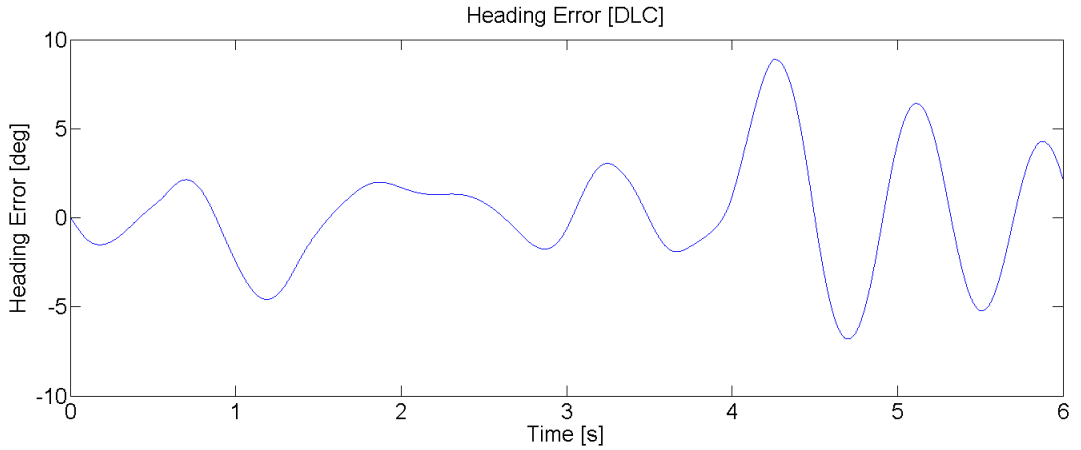

Figure 5.15: Heading error for the proposed controller during double lane change

5.3.4 Race Track

In Fig. 5.16, the outside edge of the path is shown in blue. The actual vehicle path for the proposed controller is shown in red. The vehicle path for the PID controller is shown in green. It can be observed that the PID controller does have better tracking performance than the proposed controller. However, it is expected that when the vehicle is pushed to its limit, it is difficult to stay precisely on track. The PID controller does not push the tire performance to its limits. The proposed controller aims to maximize tire performance, in trade off for error tracking. The vehicle controller by the proposed

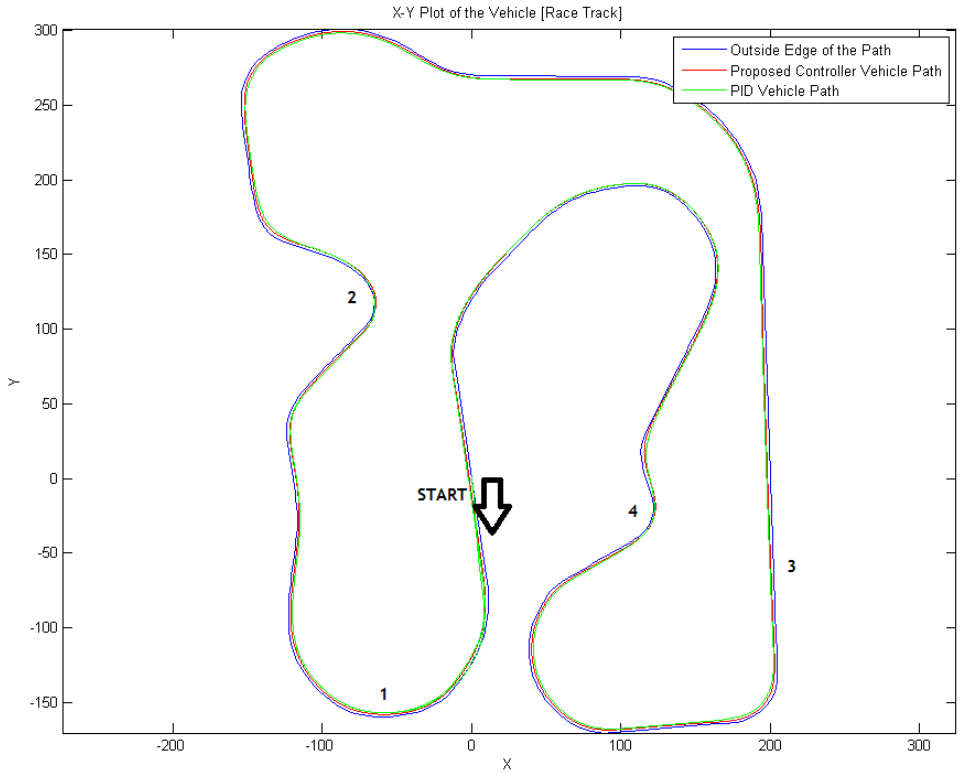

Figure 5.16: Race track positions

method follows the outside edge with a 2.25m lateral offset. It can be observed that overall, tracking performance is good; the controller is able to handle various dynamics of the road, including banking angles, elevation changes. However, the controller performed relatively poorly in four locations, the paths at these locations are very dynamic in nature, as listed below:

1. Long tight turn: prolonged change in track dynamics
2. Large S curve: introduces discontinuity in curvature
3. Long straight stretch with a sharp right corner: fast corner where speed profiling is critical
4. Small S curve: introduces discontinuity in curvature

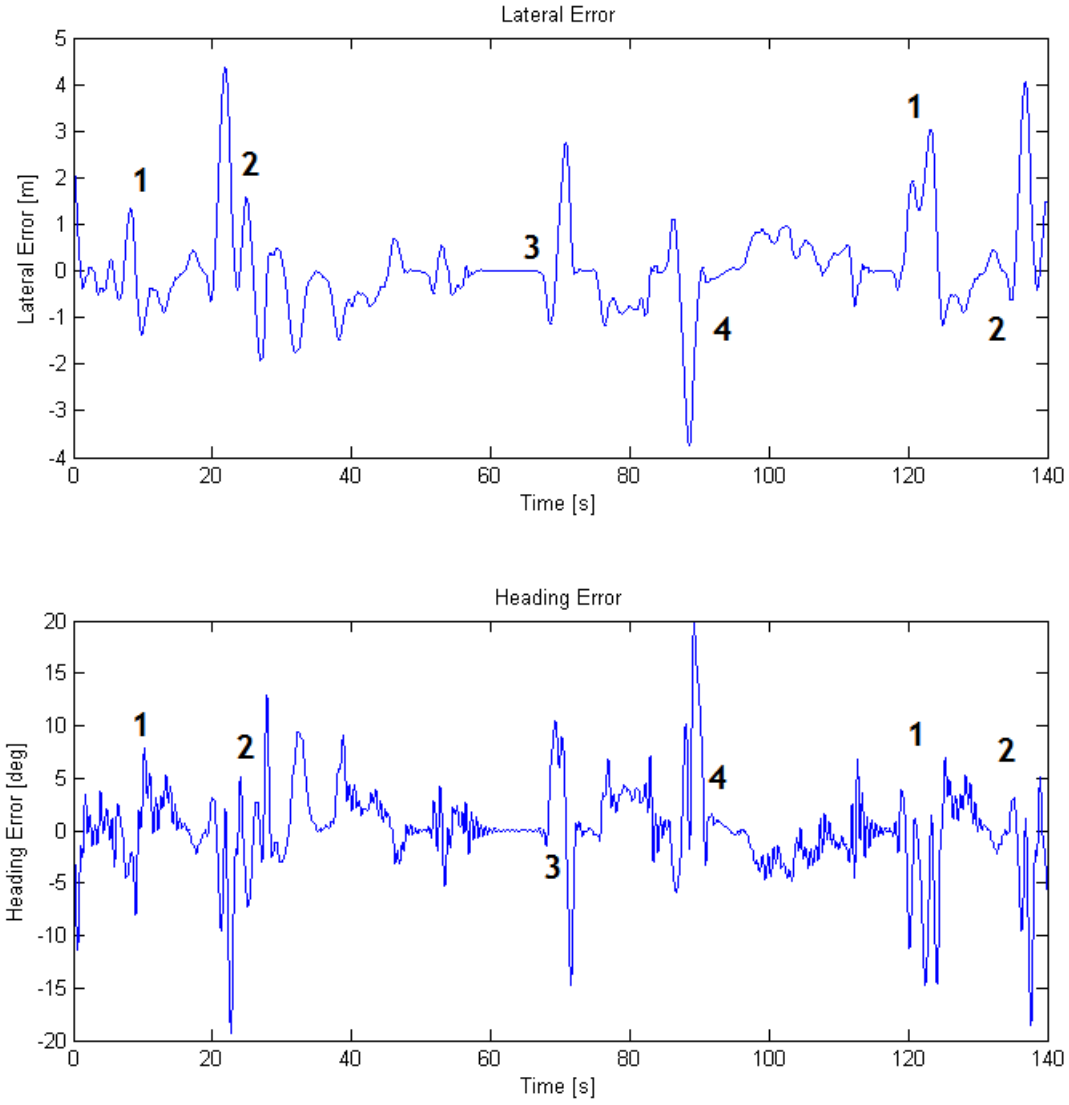

Figure 5.17: Lateral error and heading errors for the proposed controller on the race track

The lateral errors and heading errors produced by the controller are shown in Fig. 5.17. The small magnitude and consistency of the errors demonstrate that tracking performance along most of the path is good. The average lateral error in most areas are around 1m, and the average heading error is under 4 degrees. As identified above, four locations introduce some significant lateral errors: at point 1 and 3, the errors are slightly larger due to the tight turn. This is attributed to the fact that the speed profiler only uses three points to calculate the desired speed. The tight corner cannot be accurately modelled, and the desired velocity is over estimated. The vehicle must brake hard in order to make the turn, this quickly saturates the tires, and result in little lateral forces left for lateral control. At points 2 and 4, S curve, the lateral error observed is the most significant over the entire run. This is due to two reasons: firstly, there is a discontinuity in the curvature, which causes the curvature term in the feedforward lateral controller to suddenly change signs. This switch in feedforward command causes the vehicle to overreact. Secondly, with a constant radius speed profiler, the sharp changes in road direction cannot be accurately captured. The combination of feedforward command destabilizing the steering and the overestimated desired speed resulted in the large errors. As a mitigation, more points could be used to characterize road curves. This leads to a more accurate desired speed. For the same reasoning, the large errors at these four spots are also observed in Fig. 5.18. The last two peaks (not labelled) shown in the graphs are the same as point 1 and 2; when the vehicle has traversed a whole lap, and went through point 1 and 2 for the second time. It should be noted that even though larger errors are observed in certain areas, the controller performed well overall. The overall results would be even better at the four locations when a better path planner is implemented.

As shown in the longitudinal plot, Fig. 5.19, the vehicle reaches a top speed of 116 km/h along the straight stretch. In curvy areas, Point 1, 2, 4, the vehicle slows down to 40km/h to adapt to the road curvature. One area that required manual interference is from station 1375 to 1470. This is 100 meters before the end of the straight path. In this region, speed profile is manually set to 70 km/h, instead of calculated online using the speed profiler. It was noted that with only 30m look ahead distance, the vehicle cannot decelerate fast enough to go through the sharp turn. When the proper speed reference is used, the vehicle is able to go through the turn without significant deviation from the path. The speed profiles can be generated offline or online by a sophisticated planner algorithm. The simple speed profiler with only three points is not sufficient in tracking the path with twist and turns, using only 30m of look ahead distance. If the look ahead distance is increased, the curve generated by the three points would be too large, resulting in higher speeds. Since the focus is to test the capability of the controller algorithm, only a simple speed profiler is used. When proper speed profiling using multiple piece wise splines is

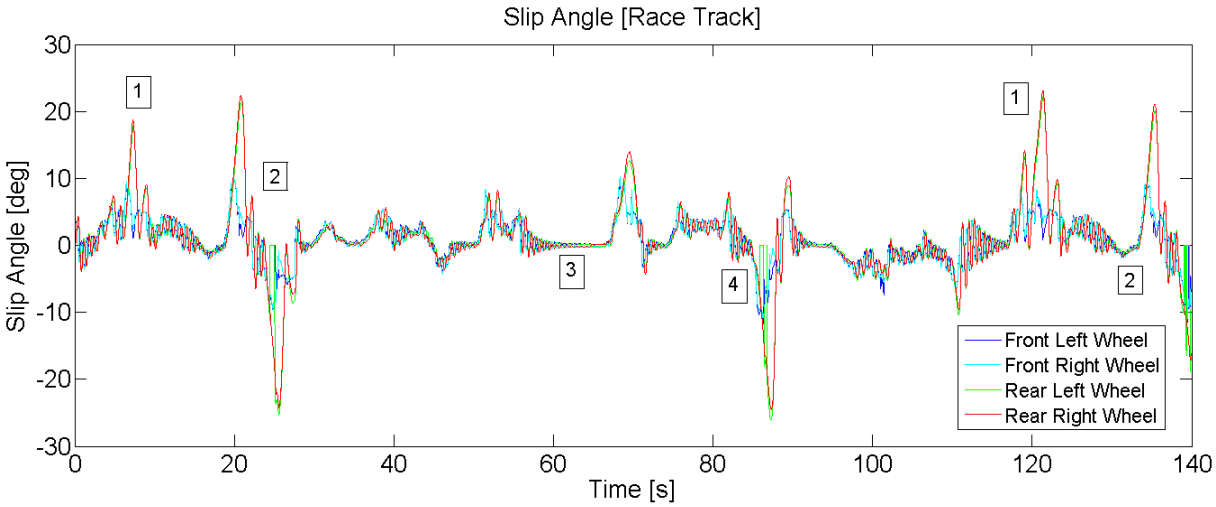

Figure 5.18: Slip angles for the proposed controller on the race track

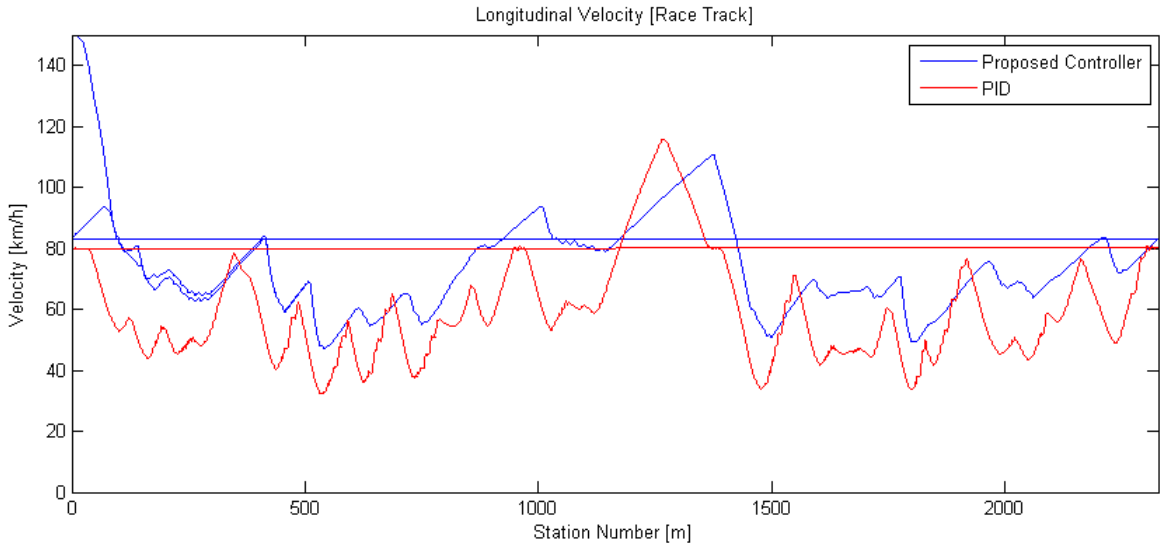

Figure 5.19: Longitudinal velocity of the vehicle along the race track

used, the vehicle can traverse through these turns without problems.

The velocity graphs of the PID controller and the proposed controller are shown in Fig. 5.19. It can be observed that the controller velocity is higher than the PID controlled vehicle in general. The average speed for the controller is 72km/h, finishing the track

in 116s, while the PID controller averages 56km/h, finishing the track in 150s. This controller is able to operate close to the friction limit, but still maintain stability. As observed, the velocities of the PID controlled vehicle and proposed controller vehicle have similar characteristics along the track. However, the PID controlled vehicle accelerates and decelerates much aggressively. While the proposed controller tends to maintain a higher, but more consistent speed. At higher speed when tire forces are saturated, there are not a lot of friction available for aggressive acceleration and deceleration while still maintaining stability. The proposed controller tends to provide consistently higher, but less aggressive speed control.

As shown in Fig. 5.20, the longitudinal accelerations are mostly between 0.1 and -0.1 m/s^2 throughout the run. This is because the longitudinal controller calculates the maximum force the tires can provide from the lateral controller, and only uses the remaining force to accelerate the vehicle. The only place where this reference is when the speed controller dominated the longitudinal forces, i.e. when the speed profile is manually set to be much lower than calculated. It can be concluded that the longitudinal controller is trying to accelerate the vehicle, and maximizing tire performance whenever it is deemed safe.

Overall, the controller introduced uses the Centre of Percussion to simplify lateral feedforward control. The longitudinal controller monitors the steering efforts, and uses the Dugoff tire model to predict the remaining tire forces, thus avoiding using the difficult to obtain slip angles. The longitudinal controller also tracks the desired speed derived from a simple speed profiler. The speed profiler is able to handle most situations, but it fails to give accurate desired speed in highly dynamic tracks. It is shown from the Circle tests that the controller is able to push the vehicle near its tire limits, and able to adapt to different tracks. Furthermore, on the very dynamic tracks, such as the Double Lane Change, the controller is still able to perform well. The performance of the controller is highly dependent on the desired speed profile. In order to improve controller performance, a more sophisticated speed profiling techniques should be used.

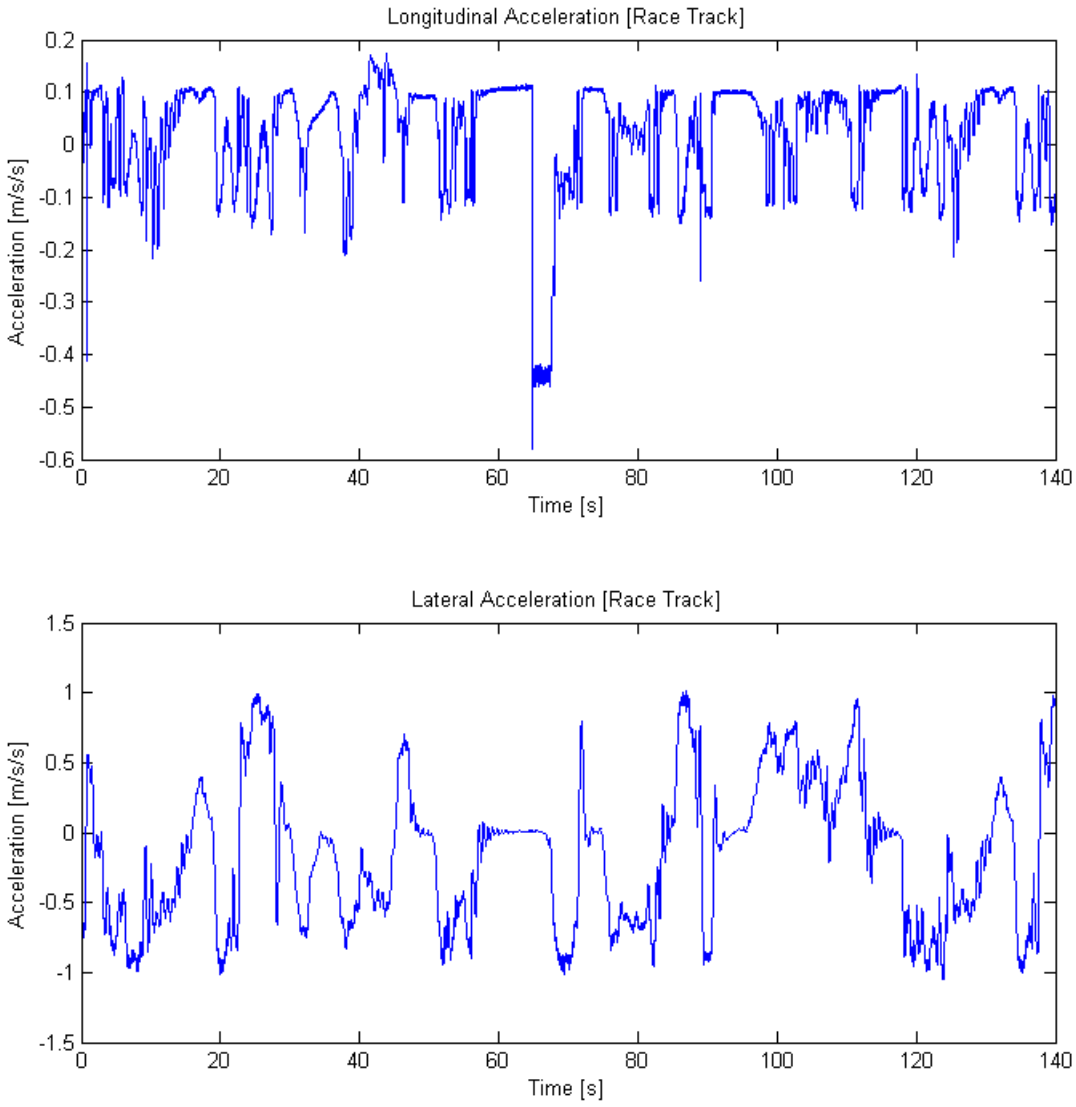

Figure 5.20: Longitudinal and lateral accelerations along the race track

Chapter 6

Conclusions and Recommendations

Recently, autonomous vehicles have became a reality: many current production cars use features that enable better autonomy and aggressive driving control. However, there are still areas that a human driver may perform better than an autonomous vehicle, and this is especially true in the field of professional racing. In racing, tires are operating near the limit of friction at all times to maximize vehicle performance. Being able to control and maintain vehicle stability in this scenario allows autonomous vehicles to be faster, and be able to handle emergency stop situations, or icy/slippery conditions much more reliably. Current research for vehicle control at the limit of friction is difficult for several reasons: one, the vehicles are usually expensive to build and maintain, two, they usually require specialized training to maintain and operate. A small scale vehicle testbed can mitigate most of these factors, while still providing validation information on vehicle control and estimation.

This thesis presents a $1/5^{th}$ scale autonomous vehicle testbed that is flexible in its hardware and software setup to accommodate various sensors for testing purposes. In order to improve the high frequency response in the steering, The steering servo is selected to be high torque and fast to minimize latency in steering. The tires are wider than a typical full scale pneumatic tire when it is scaled up. This provides faster tire responses and more traction. As a testbed for autonomous control testing, this set-up still provides valid information in the linear and near linear range of the tires, and is ideal as a initial testing platform before the controller is implemented on a full scale vehicle. In order to obtain the tire dynamics, the tires are tested under a precise IPS system. The dynamic response of the tire follows closely to that described in the Dugoff model. The C_α for the small scale tires at $\mu = 0.65$ is 5N/deg. The tests also demonstrated that pneumatic trail for the tires are noisy. It was found that the method of measuring torque based on

servo current produces a lot of noise due to the servo's internal control loop. The current measurement must either need to be heavily filtered before use, or an alternative method of determining steering torque should be used.

Determining the force interactions between the tire and the ground is crucial in controlling the vehicle near the limit of friction. Tire slip angles are especially difficult to determine. Previous work has suggested using pneumatic trail to gain additional insight into the tire dynamics. In this thesis,an expanded slip angle observed is presented which integrates a linear observer with Dugoff tire model and a pneumatic trail estimator. This design is fast to operate, and does not require expensive sensors. With the addition of the pneumatic trail block, accurate slip angles can be obtained in the tires non-slip regions. Using the Dugoff tire model, the observer is also able to accurately track slip angles into the slip region of the tire, even with a significant amount of longitudinal dynamics present. As verified by the three simulated test scenarios, this observer design consistently outperforms other common observer designs. The estimator is verified experimentally using the small scale testbed. It is determined that the observer is able to accurately determine slip angles in both the tire's linear and near non-linear region.

Vehicle control based on slip angles requires the estimator to be accurate, this is difficult to obtain for all situations, especially for a small scaled testbed. An alternative is to use forces to calculate the amount of frictional force on the tires. This thesis proposes a controller that uses a simplified feedforward lateral controller, based on the concept of Centre of Percussion. The longitudinal controller monitors the steering efforts, and uses the Dugoff tire model to predict the remaining tire forces, thus avoiding using the difficult to obtain slip angles. The longitudinal controller also tracks the desired speed derived from a simple speed profiler. The speed profiler is able to handle most situations, but fails to give accurate desired speed in highly dynamic tracks. It is shown from the Circle tests that the controller is able to push the vehicle near its tire limits, and able to adapt to different tracks. Furthermore, on the very dynamic tracks, such as the double lane change procedure, the controller is still able to perform well. The performance of the controller is highly dependent on the desired speed profile. In order to improve controller performance, more sophisticated speed profiling techniques should be used.

Several recommendations can be made on the platform and the controller: The testbed is the first step to model full size vehicle dynamics. Other low level microcontrollers, such as PIC should be investigated for its feasibility. These controllers offer more features and faster computation. Alternatively, the high level control and low level control can be combined into one real time system. Frameworks such as Open Robot Control Software (OROCOS) already exists that can integrate with ROS, while offering real time capabilities based on Linux OS. This set-up overcomes any communication throughput limitations and

communication delays. It would also simplify the hardware. Lastly, the testbed should be characterized in more scenarios with different surfaces. The experiments could validate its usability as a full scaled vehicle substitute, or could identify fixed differences between the small scaled and the full size vehicles.

In terms of the estimation method, it is useful to collect real vehicle data and verify the performance of the estimator in real test scenarios. The full size tires may introduce other dynamics, such as force lag, that may degrade the estimator performance. Without the steering servo, real vehicles may provide much better data on the alignment moment of the tires, and lead to better estimates than shown with the small scaled vehicle.

For the controller, it is recommended that a better speed profiler to be used. Many methods currently use piecewise splines to model the road ahead of the vehicle. The splines then can be evaluated to identify the smallest curvature. A desired speed recommendation can be made based on this desired speed. This would improve controller performance on straight paths and during a sharp corner.

This thesis presented three aspects of autonomous driving near the limit of friction: testbed, estimation and control. The architectures presented improve on current vehicle estimation and control methods, and pave the way for further developments on autonomous driving at the limit of friction. The future, complete with autonomous driving vehicles, is almost here.

References

[1] About ros. http://www.ros.org/about-ros/. Accessed: 2014-11-12.

[2] Watch an autonomous audi rs7 fly around the hockenheim circuit. http://autoweek.com/article/car-news/watch-audis-autonomous-rs-7-fly-around-hockenheim-circuit. Accessed: 2014-11-12.

[3] National Highway Traffic Safety Administration. National motor vehicle crash causation survey report to congress. *National Highway Traffic Safety Administration*, 811:059, 2008.

[4] Y. Aoki, T. Uchida, and Y. Hori. Experimental demonstration of body slip angle control based on a novel linear observer for electric vehicle. In *Industrial Electronics Society, 2005. IECON 2005. 31st Annual Conference of IEEE*. IEEE, 2005.

[5] E. Bakker, H.B. Pacejka, and L. Lidner. A new tire model with an application in vehicle dynamics studies. In 4^{th} *Autotechnologies Conference*, 1989.

[6] M. Bertozzi, L. Bombini, A. Broggi, M. Buzzoni, E. Cardarelli, S. Cattani, P. Cerri, S. Debattisti, R. Fedriga, M. Felisa, et al. The vislab intercontinental autonomous challenge: 13,000 km, 3 months, no driver. In *Proc. 17th World Congress on Intelligent Transportation Systems*, 2010.

[7] D.M. Bevly, J. Ryu, and J.C. Gerdes. Integrating INS sensors with GPS measurements for continuous estimation of vehicle sideslip, roll, and tire cornering stiffness. *IEEE Transactions on Intelligent Transportation Systems*, 7(4):483–493, 2006.

[8] S. Brennan and A. Alleyne. The illinois roadway simulator: A mechatronic testbed for vehicle dynamics and control. *Mechatronics, IEEE/ASME Transactions on*, 5(4):349–359, 2000.

[9] R.C. Coulter. Implementation of the pure pursuit path tracking algorithm. Technical report, DTIC Document, 1992.

[10] J. Dakhlallah, S. Glaser, S. Mammar, and Y. Sebsadji. Tire-road forces estimation using extended Kalman filter and sideslip angle evaluation. In *American Control Conference, 2008*, pages 4597–4602. IEEE, 2008.

[11] M. Doumiati, A. Victorino, A. Charara, and D. Lechner. Unscented kalman filter for real-time vehicle lateral tire forces and sideslip angle estimation. In *Intelligent Vehicles Symposium, 2009 IEEE*, pages 901–906, 2009.

[12] J. Funke, P. Theodosis, R. Hindiyeh, G. Stanek, K. Kritatakirana, J.C. Gerdes, D. Langer, M. Hernandez, B. Muller-Bessler, and B. Huhnke. Up to the limits: autonomous audi tts. In *Intelligent Vehicles Symposium, 2012 IEEE*, pages 541–547. IEEE, 2012.

[13] T.D. Gillespie. *CarSim data manual*, 2004.

[14] J. Hsu. *Estimation and control of lateral tire forces using steering torque*. PhD thesis, Standford University, 2009.

[15] Y.-H.J. Hsu, S.M. Laws, and J.C. Gerdes. Estimation of tire slip angle and friction limits using steering torque. *IEEE Transactions on Control Systems Technology*, 18(4):896–907, 2010.

[16] J.L. Jakobsen. Autonomous drifting of a 1: 5 scale model car. 2011.

[17] K. Kritayakirana and J.C. Gerdes. Autonomous vehicle control at the limits of handling. *International Journal of Vehicle Autonomous Systems*, 10(4):271–296, 2012.

[18] K. Kritayakirana and J.C. Gerdes. Using the centre of percussion to design a steering controller for an autonomous race car. *Vehicle System Dynamics*, 50(sup1):33–51, 2012.

[19] S. Lapapong, V. Gupta, E. Callejas, and S. Brennan. Fidelity of using scaled vehicles for chassis dynamic studies. *Vehicle System Dynamics*, 47(11):1401–1437, 2009.

[20] A. Liburdi. *Development of a scale Vvhicle dynamics test bed*. PhD thesis, University of Windsor, 2010.

[21] J.M. Lutin, A.L. Kornhauser, E. Lerner-Lam, et al. The revolutionary development of self-driving vehicles and implications for the transportation engineering profession. *Journal of Transportation of the Institute of Transportation Engineers*, 83(7), 2013.

[22] J. Muller. No hands, no feet: My unnerving ride in google's driverless car. *Forbes Magazine*, 2013.

[23] World Health Organization. Global status report on road safety 2013. Technical report, World Health Organization, 2013.

[24] H.B. Pacejka. *Tire and vehicle dynamics*. Butterworth-Heinemann, 2012.

[25] R. Rajamani. *Vehicle dynamics And control*. Mechanical engineering series. Springer Science, 2006.

[26] S.M. Vijaykumar R.P. Rajvardhan, S.R. Shankapal. Effect of wheel geometry parameters on vehicle steering. In *SASTech-Technical-Journal*, pages 11–18, 2010.

[27] N.D. Smith. Understanding parameters influencing tire modeling. *Department of Mechanical Engineering, Colorado State University*, 2004.

[28] J.M. Snider. Automatic steering methods for autonomous automobile path tracking. *Robotics Institute, Tech. Rep. CMU-RITR-09-08*, 2009.

[29] S. Thrun, M. Montemerlo, H. Dahlkamp, D. Stavens, A. Aron, J. Diebel, P. Fong, J. Gale, M. Halpenny, G. Hoffmann, et al. Stanley: The robot that won the darpa grand challenge. *Journal of Field Robotics*, 23(9):661–692, 2006.

[30] C. Urmson. The self-driving car logs more miles on new wheels. *Google Official Blog*, 2012.

[31] C. Urmson, C. Baker, J. Dolan, P. Rybski, B. Salesky, W. Whittaker, D. Ferguson, and M. Darms. Autonomous driving in traffic: Boss and the urban challenge. *AI Magazine*, 30(2):17, 2009.

[32] A. von Vietinghoff, M. Hiemer, and U. Kiencke. Nonlinear observer design for lateral vehicle dynamics. In *Proc. 16th IFAC World Congress*, 2005.

[33] B. Wang, Q. Cheng, A.C. Victorino, and A. Charara. Nonlinear observers of tire forces and sideslip angle estimation applied to road safety: Simulation and experimental validation. In *International IEEE Conference on Intelligent Transportation Systems, 2012 15th*, pages 1333–1338, 2012.

[34] Y. Yasui, W. Tanaka, Y. Muragishi, E. Ono, M. Momiyama, H. Katoh, H. Aizawa, and Y. Imoto. Estimation of lateral grip margin based on self-aligning torque for vehicle dynamics enhancement. *SAE transactions*, 113(6):632–637, 2004.